

RESEARCH ARTICLE

10.1029/2019JC015312

Key Points:

- Stochastic climate emulator explicitly links climate patterns to local coastal flooding components (waves, surges, sea level anomalies, etc.)
- Thousands of years of synthetic total water levels are directly simulated via individual components producing long return period event magnitudes
- Conservation of temporal structure and persistence of interannual, seasonal, and intra-seasonal time scales

Correspondence to:

D. Anderson,
 anderdyl@oregonstate.edu

Citation:

Anderson, D., Rueda, A., Cagigal, L., Antolinez, J. A. A., Mendez, F. J., & Ruggiero, P. (2019). Time-varying emulator for short and long-term analysis of coastal flood hazard potential. *Journal of Geophysical Research: Oceans*, 124. <https://doi.org/10.1029/2019JC015312>

Received 21 MAY 2019

Accepted 17 NOV 2019

Accepted article online 10 DEC 2019

Time-Varying Emulator for Short and Long-Term Analysis of Coastal Flood Hazard Potential

D. Anderson¹ , A. Rueda² , L. Cagigal^{2,3} , J. A. A. Antolinez^{2,4} , F. J. Mendez² , and P. Ruggiero⁵ 

¹Civil and Construction Engineering, Oregon State University, Corvallis, OR, USA, ²Departamento Ciencias y Tecnicas del Agua y del Medio Ambiente, Universidad de Cantabria, Santander, Spain, ³School of Environment, University of Auckland, Auckland, New Zealand, ⁴Deltares, Unit Marine and Coastal Systems, Delft, The Netherlands, ⁵College of Earth, Ocean, and Atmospheric Sciences, Oregon State University, Corvallis, OR, USA

Abstract Rising seas coupled with ever increasing coastal populations present the potential for significant social and economic loss in the 21st century. Relatively short records of the full multidimensional space contributing to total water level coastal flooding events (astronomic tides, sea level anomalies, storm surges, wave run-up, etc.) result in historical observations of only a small fraction of the possible range of conditions that could produce severe flooding. The Time-varying Emulator for Short- and Long-Term analysis of coastal flood hazard potential is presented here as a methodology capable of producing new iterations of the sea-state parameters associated with the present-day Pacific Ocean climate to simulate many synthetic extreme compound events. The emulator utilizes weather typing of fundamental climate drivers (sea surface temperatures, sea level pressures, etc.) to reduce complexity and produces new daily synoptic weather chronologies with an auto-regressive logistic model accounting for conditional dependencies on the El Niño Southern Oscillation, the Madden-Julian Oscillation, seasonality, and the prior two days of weather progression. Joint probabilities of sea-state parameters unique to simulated weather patterns are used to create new time series of the hypothetical components contributing to synthetic total water levels (swells from multiple directions coupled with water levels due to wind setup, temperature anomalies, and tides). The Time-varying Emulator for Short- and Long-Term analysis of coastal flood hazard potential reveals the importance of considering the multivariate nature of extreme coastal flooding, while progressing the ability to incorporate large-scale climate variability into site specific studies assessing hazards within the context of predicted climate change in the 21st century.

Plain Language Summary Predicting extreme coastal flooding is a present-day societal need and will only become more relevant as mean water levels increase due to sea level rise. However, the number of processes contributing to such events is too high for relatively short observational records to have measured all of the constructive combinations of waves, surge, wind, and sea level anomalies. We present a framework designed to create hypothetical combinations of relevant flood hazard potential processes by simulating the climate and weather patterns that drive coastal flooding. Including large-scale oceanic and atmospheric patterns as the drivers of coastal hazards reveals the climate a coastal community is most vulnerable to, which will be increasingly more important to understand as the climate changes during the 21st century.

1. Introduction

Global mean sea levels have risen ~3 mm/year over the last 25 years of satellite observations (Beckley et al., 2017). The observed sea level rise (SLR) has already been linked to increases in nuisance flooding (Ray & Foster, 2016; Sweet & Park, 2014), beach erosion or shoreline retreat (Albert et al., 2016; Wahl & Plant, 2015), and coastal habitat loss (Jankowski et al., 2017). A global SLR acceleration rate of 0.084 mm/year² has been observed in altimeter data since 1993 (Nerem et al., 2018), and higher rates are expected in the 21st century (Sweet et al., 2017), resulting in numerous studies focused on how the frequency of coastal hazards will increase into the future (Vitousek et al., 2017; Vousdoukas et al., 2018) as well as associated increases in vulnerable coastal populations (Neumann et al., 2015).

However, coastal flooding and erosion at any one time is dependent on the total water level (TWL; e.g., Barnard et al., 2019), which is a combination of multiple simultaneously occurring processes (i.e., wave

setup and run-up, astronomical tides, storm surges, and seasonally and climatically varying mean sea level) that exhibit variability an order of magnitude greater than the global mean SLR signal (Ruggiero et al., 2001). Each process is forced by different environmental processes (oceanographic, meteorological, and hydrological) acting at varying spatial (local to global) and temporal scales (hours to centuries; Leonard et al., 2014). Extreme water levels on beaches are underestimated without considering wave run-up and setup (e.g., Marcos et al., 2019), yet wave climates can include both local and distant swell components generated by faraway storms on the order of weeks prior to arrival (Hegermiller et al., 2017). Similarly, nontidal residuals are a product of regional wind stresses and barometric pressure anomalies occurring in the weather-band timescale, as well as regional processes such as seasonally varying upwelling and downwelling, and large-scale climate phenomena affecting basin-wide circulations (i.e., El Niño Southern Oscillation [ENSO] and Pacific Decadal Oscillation; Merrifield et al., 2012). Each of these processes are modulated by astronomic tides, which can amplify or negate the effects of an extreme weather event.

Quantifying the potential for extreme coastal conditions is thus a difficult multivariate spatio-temporal problem, which has been approached with a wide range of methodologies depending on the scope of the research effort and the resources available. A considerable body of literature is focused on the projection of future extreme sea levels within the context of uncertain global SLR from both statistical and dynamical modeling perspectives (i.e., Barnard et al., 2019; Hunter, 2011; Le Cozannet et al., 2015; Vousedoukas et al., 2016). However, uncertainties arising from commonly applied methods for quantifying present-day extremes are equal in magnitude to SLR uncertainties (Wahl et al., 2017). Traditionally, engineers designing coastal infrastructure and coastal managers defining flood zones have quantified the probability of extreme coastal flooding by applying extreme value analysis (EVA) to tide gauge records and predicting the return periods and return levels of low probability levels at a specific site (see Haigh et al., 2010 for an overview of different EVA approaches). Large uncertainties have led to the application of EVA approaches with varying degrees of complexity, including investigations of univariate or joint probability space for particular processes that a location is most sensitive to (Rueda et al., 2016), as well as applying nonstationary extreme value functions with time-dependent covariates (Méndez et al., 2006; Menéndez & Woodworth, 2010) or sliding time windows to consider non-stationary and secular trends (Wahl & Chambers, 2015).

Regardless of the statistical method, quantifying low probability events from a time series of observations is still dependent on the length of the record. Process-wise the record would ideally be long enough to have observed the full range of variability in low probability extremes. Although some observational records are suitably long enough to quantify the extremes of an individual process, the compound TWL extremes resulting from multiple low-probability events co-occurring requires much longer records than currently available in observations. Multiple methods have been developed to avoid the problem of historical water level record lengths while incorporating extreme value theory. Probabilistic methods utilize Monte Carlo simulations of individual probability distributions for each TWL component to derive artificial or synthetic records more suitable for EVA (Callaghan et al., 2008; Gouldby et al., 2014; Serafin & Ruggiero, 2014; MacPherson et al., 2019). Hybrid methods composed of both synthetically extended storm characteristics and subsequent hydrodynamic modeling have been proposed for coastlines susceptible to large storm events (Haigh et al., 2014). Other efforts have taken advantage of ever-increasing computational powers to numerically hindcast longer records at regional and global scales (i.e., Muis et al., 2016; Vitousek et al., 2017), with the advantage of deriving both spatial variability in extremes and accounting for the non-linear interactions between TWL components.

Unfortunately, the issue of record lengths is also applicable to the climate and weather which produced historically observed TWLs. Observational records have only captured a limited number of slowly varying climate oscillations, but correlations between extreme coastal conditions and specific interannual climate indices have been found around the world (Barnard et al., 2015; Plomaritis et al., 2015). In terms of the resulting sea levels, Wahl and Chambers (2015) and Marcos et al. (2015) used independent methods to both find interannual to multidecadal trends of tide gauge-derived extreme sea levels that exhibited regional coherence, suggesting large-scale climate drivers are an important modulator of the probability of coastal flooding. Although general circulation models (GCMs) can provide an ensemble of possible future changes in large-scale teleconnections and associated extreme coastal conditions (e.g., Mentaschi et al., 2017), questions remain regarding our understanding of present-day extremes and their dependence on a single observation of stochastic climate and weather. How variable could our observational record of coastal

TWLs be if different yet equally plausible sequences of climate oscillations and weather had aligned differently with the tides? Are statistical uncertainty bounds derived from EVA approaches representative of the range of variability resulting from a stochastic natural world?

This study proposes a methodology for simulating synthetic records of large-scale climate forcing, generating plausible progressions of synoptic weather patterns conditioned on the large-scale forcing, and ultimately deriving artificial records of the multivariate drivers of potential coastal flooding. The Time-varying Emulator for Short- and Long-term Analysis of coastal flood hazard potential (TESLA-flood) is intended to better constrain the extrapolation of extreme coastal water levels while maintaining an explicit link between climate phenomena and the resulting local components of TWLs. Time-dependent probabilities due to seasonal, interannual, and long-term oscillations within the climate system are accounted for, ultimately creating a framework capable of simulating thousands of years of a representative climate to generate potential combinations of hydrodynamic boundary conditions which produce sea level variability not necessarily observed in the historical record. The climate emulator is applied to wave and water level observations on an open coast sandy-beach in San Diego, CA described in section 2, necessitating the climate emulator be built on phenomena relevant to the eastern Pacific Ocean (described in section 3 and the Appendix). Simulating hourly time scales is accomplished by reducing the multivariate historical observations to a single parameter (TWLs) with temporal behavior and subsequently increasing the parameter space using historical joint-probabilities (described in section 3). Example time series produced by the emulator are provided in section 4, including a demonstration of extreme events with respect to both constitutive components and the large-scale causal climate. Sensitivities, limitations, and the potential for future methodological developments are addressed in section 5.

2. Wave and Water Level Components in San Diego, CA

The stochastic climate emulator developed in this study is applied to an open coast sandy-beach setting in San Diego, CA, USA. The westward facing beach is composed of 0.20 mm grain size sand on an average 0.03 slope (Ludka et al., 2015), exposed to annually averaged 2.25 m deep water waves (seasonally varying with smaller waves in summer, larger in winter), and a diurnal meso-tidal range. Observations of the still water level (SWL) were obtained from National Oceanic and Atmospheric Administration tide gauge 9410230 located on the open coast at a pier in La Jolla, CA (Figure 1). The SWL was separated into its constitutive components using the frequency domain-based approach developed by Serafin and Ruggiero (2014):

$$SWL = \eta_{MSL} + \eta_A + \eta_{SE} + \eta_{MMSLA} + \eta_{SS} \quad (1)$$

where η_{MSL} is the mean sea level relative to some reference datum, η_A is the astronomical tide, η_{SE} is an intra-annual seasonal water level variation, η_{MMSLA} is the monthly mean sea level variability, and η_{SS} is the storm surge signal resulting from atmospheric pressure variability and wind setup. Local land subsidence in southern California has contributed to a mean SLR of 2.2 mm/year since 1924. Seasonal SWL variability of ± 8 cm, with a minimum in April and a maximum in September, is due primarily to seasonal upwelling of cool deep-ocean water masses. The largest MMSLA events occurred during canonical El Niño years such as 1982–83, 1997–98, and 2015–16 when 20–30 cm of elevated water levels persisted for months due to warm water anomalies propagating from west to east across the equatorial Pacific Ocean.

Coastal erosion during these El Niño years was severe, as winter storms produced anomalously high waves and run-up on top of the elevated mean water surface (Barnard et al., 2017; Ludka et al., 2016). Run-up was calculated using the empirical formulation of Stockdon et al. (2006):

$$R_{2\%} = 1.1 \left(0.35\beta(H_s L_0)^{0.5} + \frac{[H_s L_0 (0.563\beta^2 + 0.004)]^{1/2}}{2} \right) \quad (2)$$

where H_s and L_0 are the deep-water wave height and wavelength, respectively, and β is the beach slope. Together, the still water level and run-up can be combined to create a TWL:

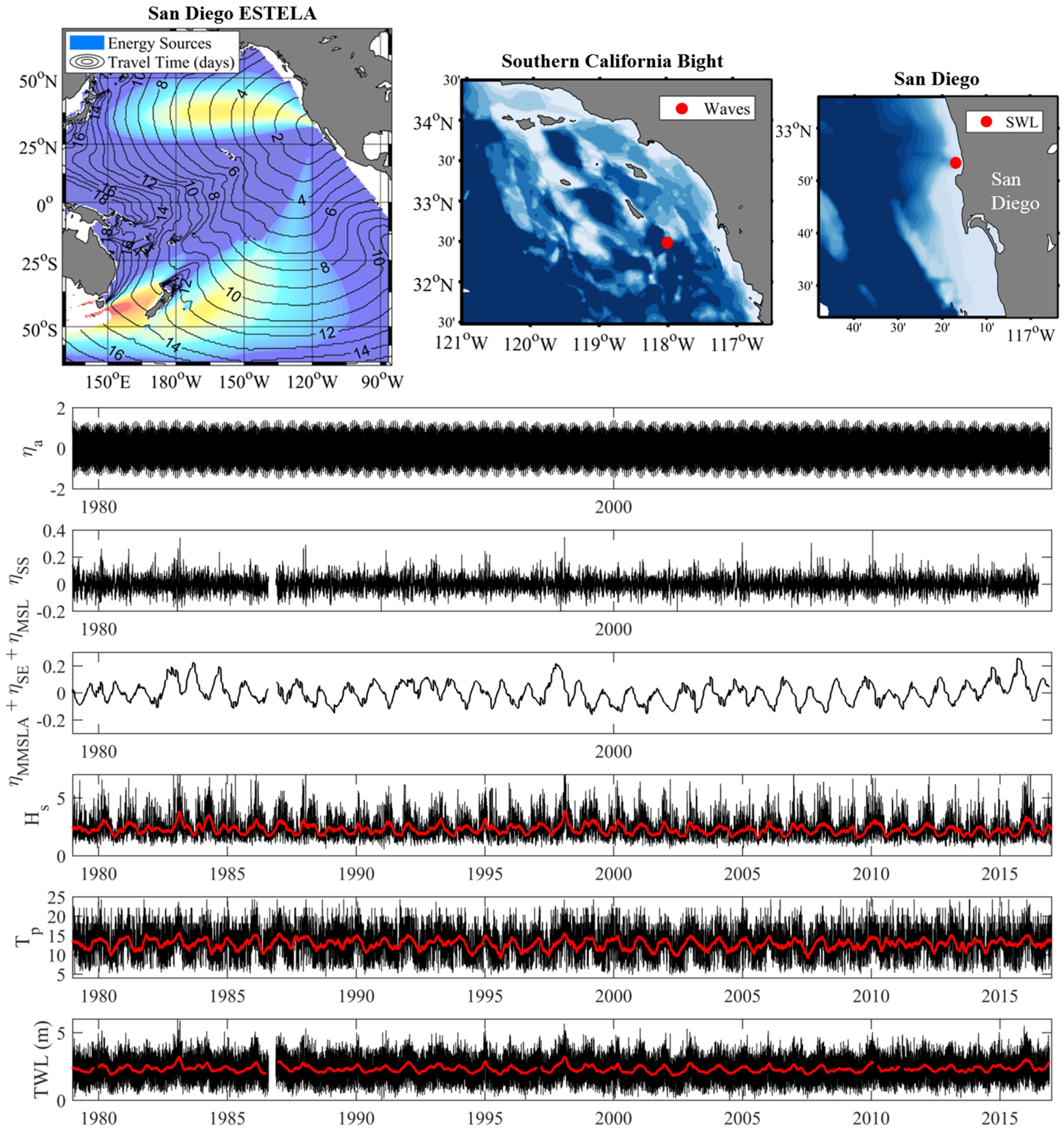


Figure 1. (a) The Pacific Ocean with wave energy sources relevant to San Diego denoted by averaged travel time for waves to propagate in days. Insets denote the wave node and SWL gauge used for wave and water level time series provided in (b–f), and the cumulative TWL in (g). Black lines denote hourly values while red lines are 2-month moving averages.

$$TWL = SWL + R_{2\%} \quad (3)$$

which provides an approximation for the elevation on the beach that water is interacting with and potentially eroding (Ruggiero et al., 2001; Sallenger, 2000).

$R_{2\%}$ values contributing to the TWL calculated in Figure 1 assume the locally averaged beach slope, neglecting seasonal variations and trends in beach morphology. Thus, the predicted elevation of TWLs is a proxy for coastal flood hazard potential at the study site. The empirical equation in (2) uses deep-water wave characteristics, which were obtained from a global ocean wave (GOW2) hindcast between 1979 and 2015 produced by a multigrid WaveWatchIII model forced with hourly winds from the Climate Forecast System Reanalysis (CFSR) and validated and bias-corrected with buoys and altimeter data (Perez et al., 2017). The wave-node used here is in 1,200 m of water southwest of San Diego (Figure 1a). Automated identification of wave spectrum partitions representative of swell waves from the northern hemisphere (NH) Pacific, southern hemisphere (SH) Pacific, and local coastal ocean sea waves was performed following Rueda, Hegermiller, et al. (2017) (hereinafter referred to as *NH*, *SH*, *SEA*).

3. Developing a Stochastic Climate Emulator

The stochastic climate emulator proposed in this study is built on the recognition that coastal conditions are the result of meteorological forcing, and that synoptic-scale meteorology is in turn a consequence of large-scale quasi-steady atmospheric and oceanic patterns (e.g., Hannachi & Legras, 1995). Figure 2 provides a conceptual diagram of the emulator as a downscaling framework linking climate patterns at multiple time scales to plausible sequences of daily weather patterns and ultimately daily variability in TWLs. The emulator is built on conditional dependencies between climate patterns identified via weather-type (WT) classifications (see Appendix A for details regarding automated classification methods, and github page <https://github.com/teslakit/teslakit> for open-source codes used in this work). This statistical downscaling allows for computationally fast simulations of time-dependent stochastic weather progression conditioned on time series of large-scale forcing. WTs were classified at the annual-scale (AWTs), the intra-seasonal scale (IWTs), and the daily-scale (DWTs). In the demonstrated application to San Diego, six AWTs are used to represent the El Niño Southern Oscillation (ENSO), which is an asymmetric cycle of warm surface waters moving across the equatorial Pacific Ocean that dominates interannual variability and exhibits teleconnections known to affect weather around the world (Philander, 1983; see Appendix A.1.). IWTs are representative of the Madden-Julian Oscillation (MJO), which is a broad region of anomalous atmospheric circulation and convective precipitation anomalies that propagates eastward around the equator on 1- to 2-month time-scales (Madden & Julian, 1972) and exhibits correlations with relevant coastal climatology such as tropical cyclone (TC) genesis (Slade & Maloney, 2013) and surface wind wave anomalies (Marshall et al., 2015, Godoi et al., 2019; see Appendix A.2.). These two climate oscillations were chosen due to their relevance at San Diego but conceptually are modular pieces of the emulator that could be replaced with other climate indices representative of dominant forcing at sites elsewhere in the world.

Synoptic weather was classified on a daily scale using sea level pressures (SLPs) and gradients of SLPs observed since 1979 in regions of the Pacific that generate both swell and wind waves relevant to the study site (see Appendix A.3.). TC generation days were withheld from the WT-classification a priori and instead classified within six different DWTs depending on the ultimate strength of the TC (depression plus categories 1 through 5). All remaining days were classified into 36 extra-tropical DWTs, each representative of a cluster containing at least 100 days with similar weather from the historical record. The 42 DWTs are presented in Figure 3a as a matrix analogous to a self-organized map (Sheridan & Lee, 2011) to ensure that DWTs with similar spatial patterns are graphically presented adjacent to each other. Figures 3b–3d demonstrate how DWTs have historically exhibited conditional dependencies on the state of large-scale climate phenomena. The most readily discernable conditional dependencies are on seasonal scales (Figure 3d) where most DWTs exhibit a high probability of occurrence during a particular season and zero chance of occurring at other times. Although DWT dependencies on IWTs and AWTs are not as stark, probabilities of daily weather are still clearly affected, most notably with difference between the extremes of El Niño/La Niña (Figure 3b) and when the MJO is located on opposite sides of the globe (Figure 3c).

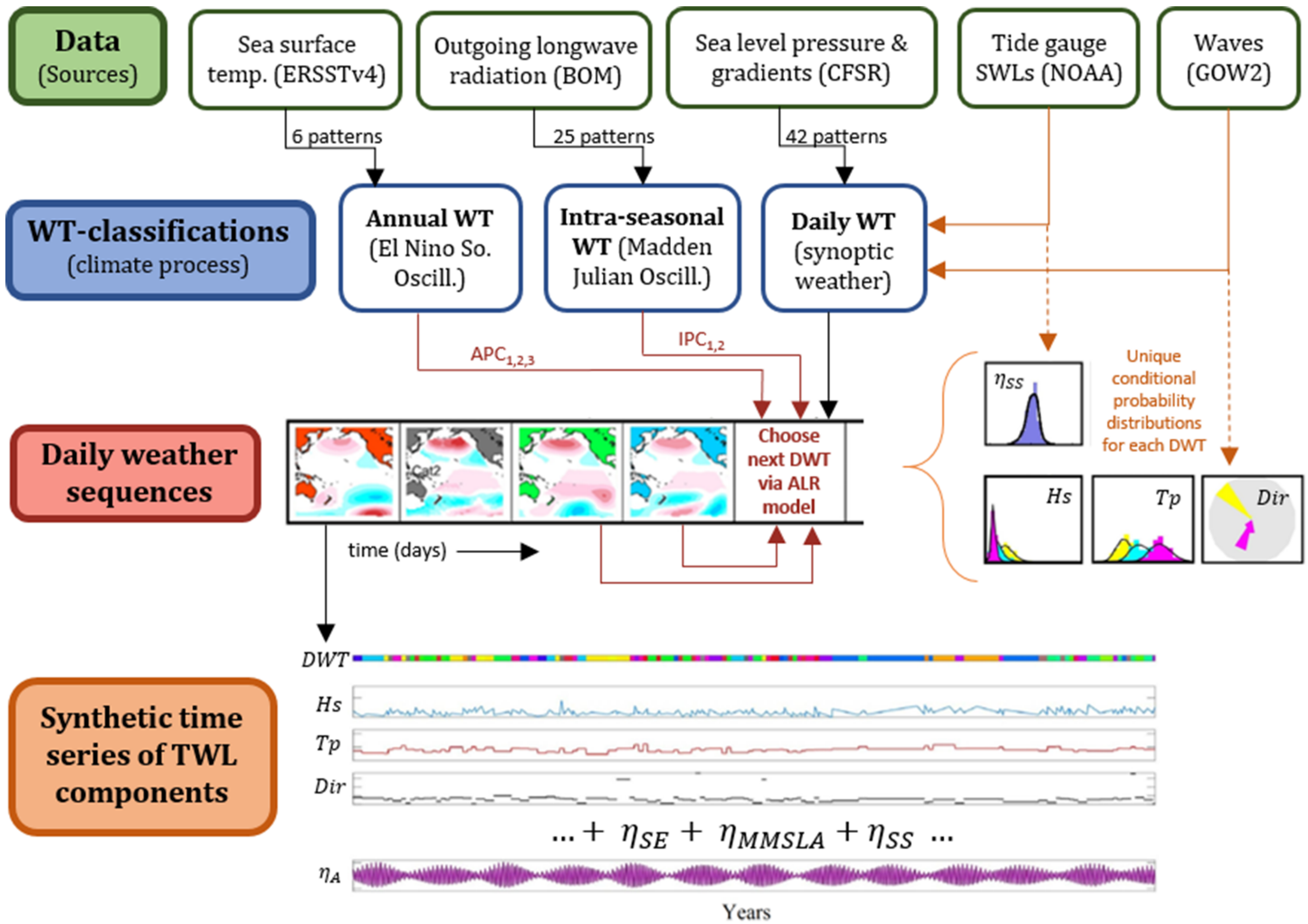


Figure 2. Conceptual flow diagram of the stochastic climate emulator. Multiple datasets (green) are classified via weather-typing at various time scales (blue) to identify common patterns that persist within large-scale climate oscillations. An ALR model is then fit to covariates from the WTs and used to simulate synthetic time series of weather (red). Unique distributions of TWL components are identified for each DWT (orange) and randomly sampled from Gaussian copulas to generate synthetic time series of local coastal forcing (bottom rows).

3.1. ALR Model for DWT Sequencing

Simulating sequencing and persistence of synthetic DWTs is accomplished with an autoregressive logistic model (ALR). ALR models are simultaneously able to account for covariates varying at different timescales as well as the autocorrelation of those covariates at different orders (Antolinez et al., 2015; Chiri et al., 2019; Guanche et al., 2013). In this sense, the AWT, seasonality, IWT, as well as the ordering (transitions between DWTs) and duration (persistence within a DWT) can all be accounted for within a single framework to make a categorical decision of what the weather pattern should be on any given day. Mathematically, the model is represented as:

$$\text{Prob}(Y_t = i | Y_{t-1}, \dots, Y_{t-e}, X_t) = \frac{\exp(\beta_{0,i} + \beta_{1,i}\cos(\omega t) + \beta_{2,i}\sin(\omega t) + \sum_{j=1}^3 \beta_{j,i}^{\text{awt}} \text{APC}_j(t) + \sum_{j=1}^2 \beta_{j,i}^{\text{iwt}} \text{IPC}_j(t) + \sum_{j=1}^e Y_{t-j} \gamma_{j,i})}{\sum_{k=1}^{n_{\text{DWT}}} \exp(\beta_{0,k} + \beta_{1,k}\cos(\omega t) + \beta_{2,k}\sin(\omega t) + \sum_{j=1}^3 \beta_{j,k}^{\text{awt}} \text{APC}_j(t) + \sum_{j=1}^2 \beta_{j,k}^{\text{iwt}} \text{IPC}_j(t) + \sum_{j=1}^e Y_{t-j} \gamma_{j,k})}$$

where covariates $\beta_{1,i}$ and $\beta_{2,i}$ account for seasonal probability of each weather type i defined by sines and cosines with 12 month periods, covariates $\beta_{j,i}^{\text{awt}}$ account for each weather type's probability associated with the leading three principle components used to create the AWTs (see Appendix A.1.), covariates $\beta_{j,i}^{\text{iwt}}$

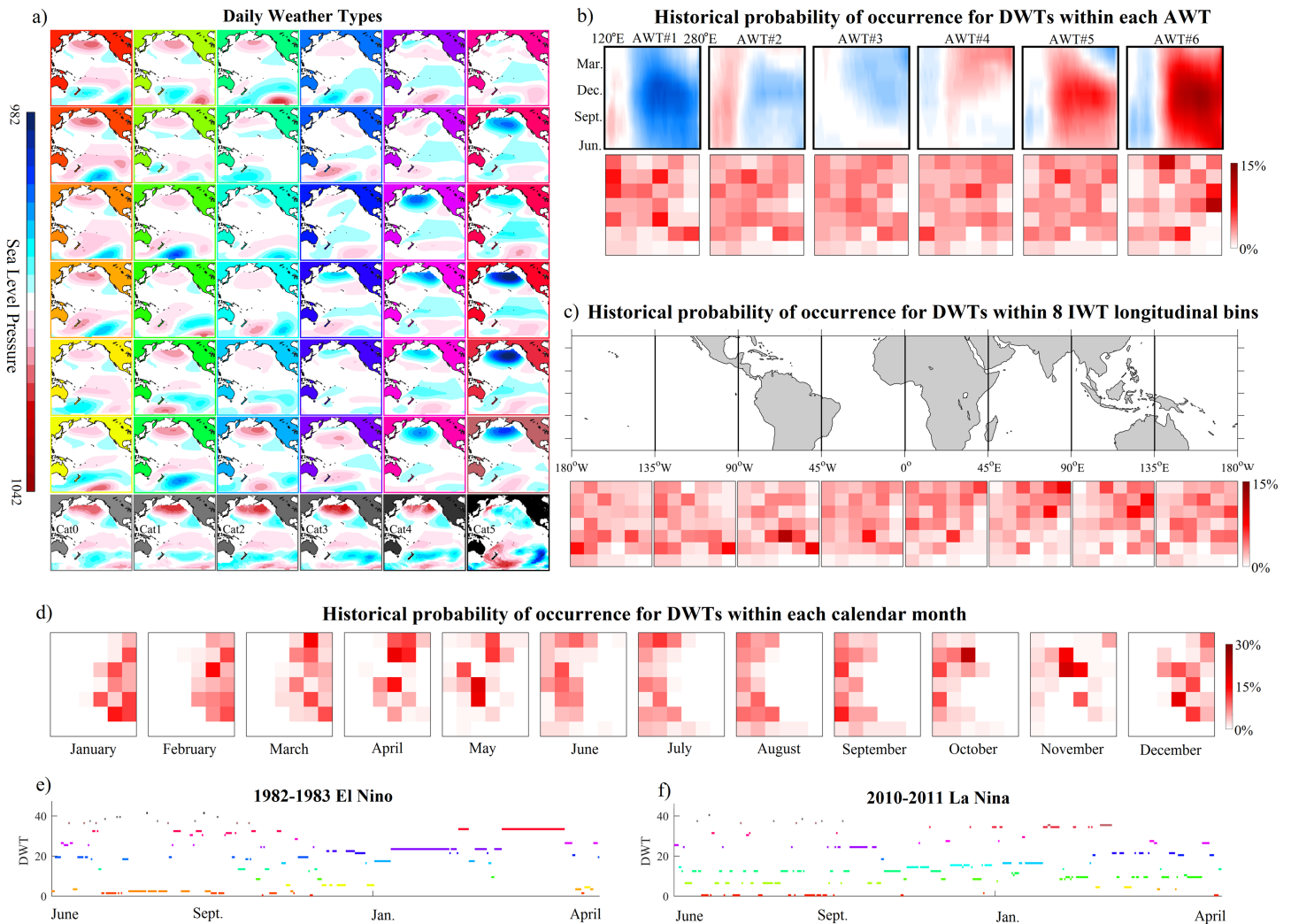


Figure 3. (a) The 42 DWTs (36 synoptic weather patterns in color +6 tropical cyclone genesis DWTs in grayscale) graphically presented in a 7×6 matrix via a self-organized map such that patterns with similarities are presented adjacent to each other (note the large low pressures in the North Pacific grouped along the right-hand side of the matrix). (b) The 6 AWT patterns are presented in a 7×6 checkerboard immediately beneath denoting the probability of DWT in (a) occurring during historical years classified as that AWT. (c) Similar to (b), a 7×6 checkerboard for the probability of DWTs occurring when the IWT is classified in eight different longitudinal bins. (d) A 7×6 probability checkerboard for each month to highlight that DWTs on the left side in (a) occur during the summer and fall while DWTs on the right side of the matrix occur during winter. Example classifications are provided for the weather observed during (e) the 1982–1983 El Niño and (f) the 2010–2011 La Niña with color of the bar indicating which weather pattern in (a) was present during the boreal winters.

account for the leading two principle components of the MJO (see Appendix A.2.), and Y_{t-j} represents the DWT of the previous j -states, $\gamma_{j,i}$ is the parameter associated with the previous j -state, and the order e corresponds to the number of previous states that influence the actual DWT. Each of these covariates was found to be statistically significant by the likelihood ratio (Guanche et al., 2013), where inclusion of a covariate required an improvement in prediction beyond a penalty associated with the added degrees of freedom. An iterative method began with the best univariate model (seasonality) and added each covariate in a pair-wise fashion to determine the next best model (seasonality + IWT_2), continuing this process until all covariates were added. This method determined the relative importance of the covariates beginning with most relevant to be seasonality, IWT_2 , IWT_1 , AWT_1 , AWT_2 , and AWT_3 .

The ALR model's ability to produce realistic synoptic weather was validated by simulating 100 synthetic iterations of DWT chronologies forced with 39 years of historical AWT and IWT. The observed probability of occurrence is directly compared to the mean and standard deviation of simulated probabilities in

Figure 4a, and the average change in transition probabilities between each DWT and every other DWT is provided in Figure 4b. The greatest difference in Figure 4b is 3.7% change between observed and simulated, suggesting the model can reproduce not just overall occurrence but also the sequencing between DWTs resulting from the Markov chain.

Although the bulk statistics are preserved by the emulator, Figures 4c–4e are provided to demonstrate that the ALR model can be forced by the same input but produce uniquely different time series of DWTs, thus simulating the stochastic nature of synoptic weather. Extended synthetic records of AWTs and IWTs (see Appendix A) allow for longer simulations of DWTs while also introducing new realizations of ENSO and superimposed MJO activity not observed in the historical records (Figure 4f). Figure 4 is designed to most readily identify the seasonal variability, but such longer time series also reveal subtle dependencies on large-scale climate that are much more difficult to quantify in the historical record. As an example, the intra-annual probability of DWT occurrence on any given day during the year is conditionally dependent on the presence of El Niño and La Niña (note overall differences in orange DWTs during summer, and blue DWTs during winter in Figures 4g–4h).

3.2. Simulating Waves and Water Levels

Associating each synthetic iteration of synoptic weather with hypothetical local environmental parameters is a multi-step process, which emphasizes preservation of joint probability across multiple variables while maintaining flexibility for high dimensionality (Figure 5). Examples provided hereinafter are focused on waves and water level output relevant to the calculation of TWLs, but the full dimensionality includes additional output with respect to atmospheric SLP, wind magnitude and direction, and precipitation. The methodology is based on the concept that sequences of consecutive daily weather typically contain the same synoptic weather system, and that the potential for flooding is maximized at some point during that weather system. In the automated classification of DWTs, this spatial correlation results in several days in a row often being assigned the same representative cluster. Consecutive days of the same DWT are grouped together and considered in this study to be a single weather system approaching and passing over San Diego, with associated ramp-up and ramp-down of sea-state parameters (Figure 5). By defining persistent DWTs as hydrographs, the 39-year DWT historical record, containing 14,625 days, reduces to 6,614 separate hydrographs. The potential for water level in excess of the tide, MSL, and MMSLA was defined by:

$$TWL_{\text{proxy}} = R_{2\%} + SS$$

where the first term on the right-hand side is the proxy for run-up introduced in section 2 (Rueda et al., 2016; Stockdon et al., 2006). All sea-state parameters at the time of maximum TWL_{proxy} during each hydrograph were used to create distributions unique to each DWT (Figure 6). The idealized sketch in Figure 5 demonstrates that this approach does not always identify the maximum value of each parameter (which often occur at different times, e.g., Serafin & Ruggiero, 2014). Instead the goal here is to preserve physically realistic joint dependence of sea-state parameters, while reducing the problem to a parameter independent of the deterministic tides.

The fourth row of the DWT matrix provided in Figure 3a is repeated in Figure 6, with each DWT's associated sea-state parameter distributions provided to demonstrate how the automated identification of atmospheric variability also delineated variability within the local TWL components. Weather patterns identifying large low-pressure systems in the north Pacific Ocean contain large, long period swells from the north (right-hand columns in Figure 6), while patterns with large SH storms identify times when swells from the south dominate wave energy (left-hand columns in Figure 6). This effectively means that the daily atmospheric, SLP field predictor is able to identify the distant storm events responsible for swell waves arriving to San Diego, and that the objective classification of clusters is able to downscale the large-scale climate variability to local sea-state variability.

The probability of *NH*, *SH*, and *SEA* components being present (1) or not present (0) at the time of observed peak TWL_{proxy} was used to create eight potential sea-states within each DWT (000, 100, 010, 001, 110, 101, 011, 111) defined by Bernoulli distributions (Rueda, Hegermiller, et al., 2017). For each hydrograph produced in the simulations of climate, a random pick from the appropriate Bernoulli distribution determined which sea state was present during that hydrograph. A subsequent random pick from the assigned sea state's

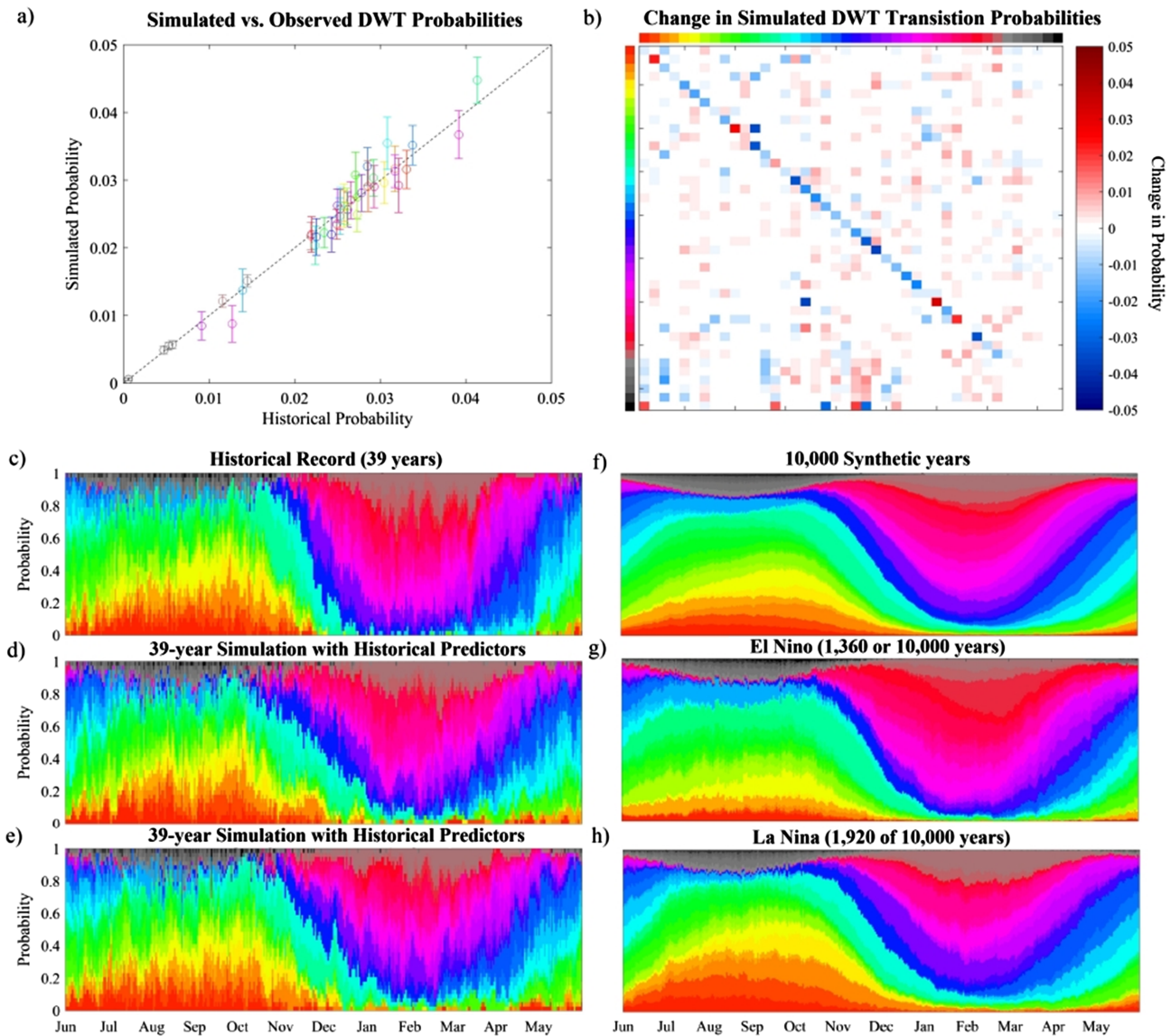


Figure 4. Evaluation of synthetic DWT simulations compared to historic behavior. (a) The color definitions for each DWT in Figure 3a are used to compare observed historical probability of occurrence to the mean probability and standard deviation across 100 simulations of the historical large-scale forcing. (b) The percent change between observed and average simulated transition probabilities. The 42 colored boxes along each axis denote the 42 DWTs as defined in Figure 3a. Each row provides the percent change of a particular DWT (denoted by color to the left of the row) transitioning to every other DWT (denoted by the color at the top of the column). (c) Conditional probability of each DWT expressed by stacked color bars for the historical observations between 1979 and 2018 compared to (d) and (e) two different simulations of DWTs driven by the same historical AWT and IWT predictors to highlight the stochastic nature of the simulations. (f) 10,000 years of synthetic AWT and IWT predictors reveal each DWT's average relative probability as captured by the ALR model. Conditional dependence of DWTs on (g) El Niño (AWT#6) and (h) La Niña (AWT#1) provide further context for the effect that the large-scale climate drivers have on the daily synoptic weather's probability of occurrence.

marginal distributions defined the waves and water levels at the maximum TWL peak within the simulated hydrograph.

The marginal distributions of waves and surge levels were associated with each other using multivariate Gaussian copulas (Rueda et al., 2016). The copulas define the dependence structure or joint probabilities between each environmental parameter within a sea state by identifying correlation matrices after transforming each marginal distribution to a uniform distribution. Identifying the correlation across all parameters through the copulas ensures that realistic combinations of compounding environmental parameters are present in the hypothetical time series (i.e., large storm waves approach from appropriate

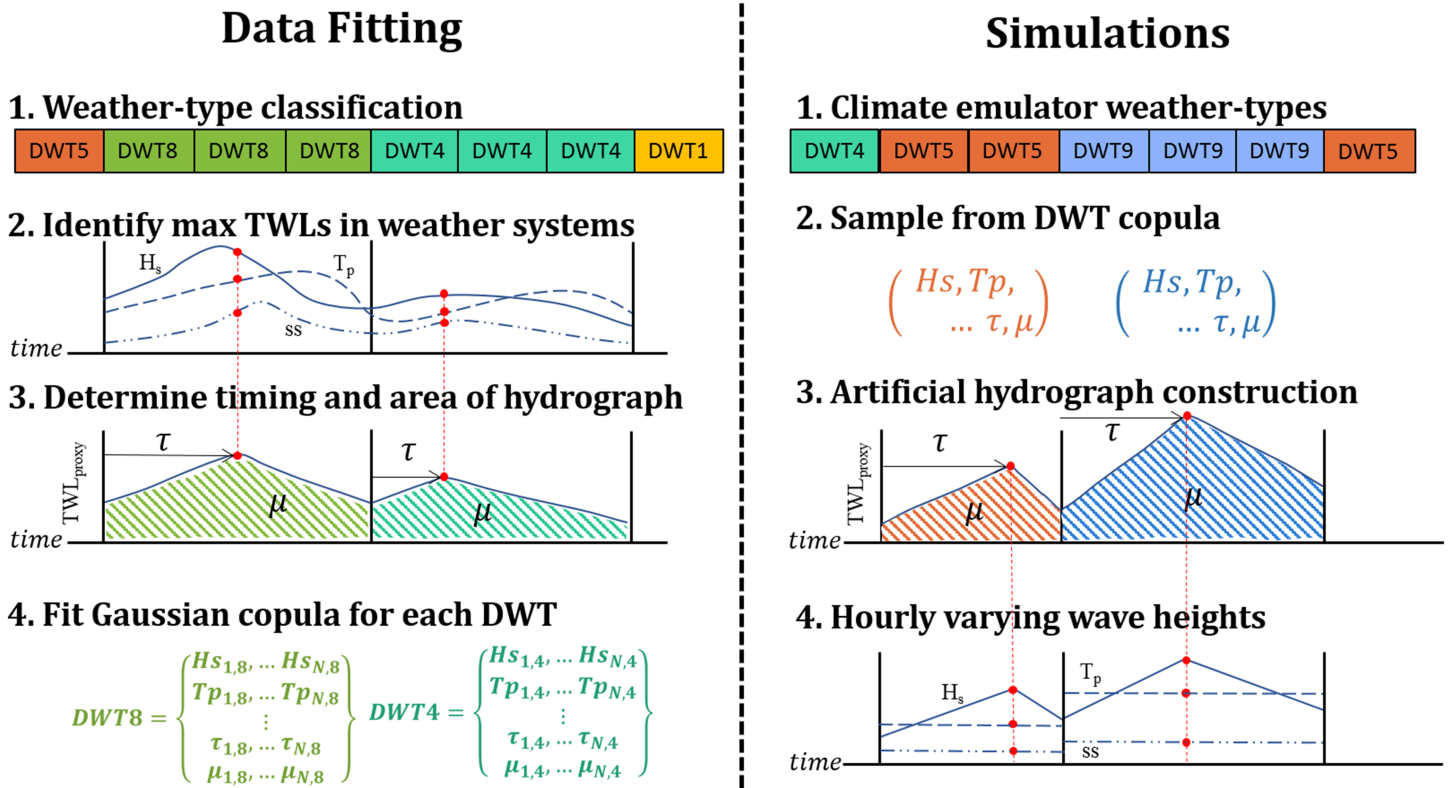


Figure 5. Definition sketch for generating Gaussian copulas of historic sea-state parameters identified as conditions at the maximum flooding potential during each weather system (producing the distributions provided in Figure 6). The copulas are then used to create synthetic hydrographs during simulations of synthetic atmospheric variability.

wave directions; Masina et al., 2015; Corbella & Stretch, 2013). The marginal distributions of wave heights and storm surge levels were defined by GEVs to allow for simulation of extremes with longer return periods than the observation period, while wave periods and directions were defined by empirical distributions constructed from observations (Huang et al., 2008; Rueda, Vitousek, et al., 2017).

Additional parameters including τ (timing of the peak TWL within a hydrograph) and μ (area under the hydrograph) were also added to each copula and randomly sampled for each simulated hydrograph. The two parameters effectively define a trapezoidal shape for each simulated hydrograph with the final TWL of each hydrograph used as the initial boundary condition for the following hydrograph (see Figure 5, analogous to the storm schematization of other recent works, e.g., Poelhekke et al., 2016). Including these parameters in the copulas accounts for correlation between storminess and hydrograph shape (peaky hydrographs are commonly associated with storm conditions while more flat hydrographs typically occur during calmer conditions). The shape of the simulated hydrograph was then used to interpolate to an hourly value of the TWL_{proxy} , and subsequently to an hourly value of wave and surge conditions (for simplicity, storm surge, wave directions, and wave periods were assumed constant within each hydrograph while wave height was allowed to vary to produce hourly TWL_{proxy} predictions).

3.2.1. SWL Variability

Monthly sea level variability is typically due to processes occurring at longer timescales than the daily weather. Slowly varying seasonality and anomalies due to ENSO are retained in the climate emulator via the principal components (PCs) used to develop the AWT (Appendix A.1.). A multivariate regression model containing a mean plus annual and seasonal cycles at 12-month and 6-month periods for each APC covariate was fit to the $\eta_{MMSLA} + \eta_{SE}$ signal at San Diego (Figure 7). This simple model explains ~75% of the variance without any specific information regarding local conditions (i.e., local anomalies due to coastal shelf dynamics, local SSTAs, or local atmospheric patterns, Sheridan et al., 2019) and slightly underpredicts extreme monthly sea level anomalies by ~10 cm. While this component of the approach is a subject of

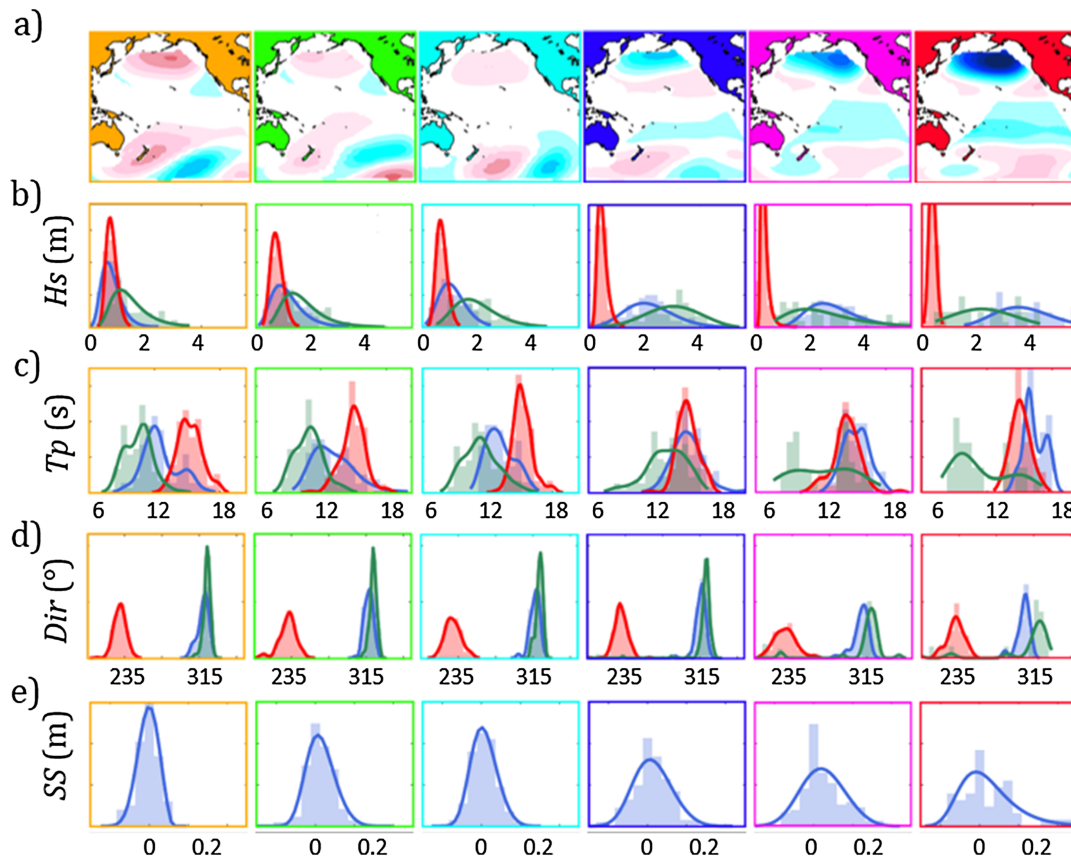


Figure 6. (a) The DWTs from the fourth row of Figure 3a are provided with univariate distributions of their (b) significant wave heights, (c) peak wave periods, (d) mean wave directions, and (e) storm surge occurring at the peak of TWL hydrographs. In b–d waves from the *SH* are in red, from the *NW* are in blue, and *SEA* is in green. Wave heights and storm surge have been fit with GEVs, while wave periods and directions are empirical distributions.

ongoing research, the regression model produces an additional ~ 0.35 m of regional SWL variability about mean sea level, which was deemed sufficient for the purposes of demonstrating the development of the stochastic climate emulator.

Superimposed on top of all other variables is the deterministic tide signal. Tides were simulated by determining the leading 64 constituents using the T_Tide package applied to observed water levels at La Jolla, CA (Pawlowicz et al., 2002). Superimposing the predicted tides as an independent process still inherently accounts for the timing of events during the calendar year (i.e., king tides in January and February due to Earth’s orbital position are associated with realistic winter weather patterns produced by the emulator). Tide time series were simulated at present-day mean sea level. Incorporating future SLR into the presented framework is straightforward and the subject of ongoing work.

4. Climate Emulator TWL Output

The complete stochastic climate emulator produces output time series for each of the parameters necessary to calculate a TWL by equations (1), (2), and (3). Example output is provided in Figure 8, including synthetic climate predictors (Figures 8a and 8b), the resulting synoptic weather (Figure 8c), and time series of the environmental parameters contributing to creating compound TWLs (Figures 8d–8i). The demonstration here is with a 100-year simulation to aid in visualizing timescales of variability in individual components; however, the methodology can produce output at any desired time scale (decades to thousands of years). In this example, the wave components from the *NH*, *SH*, and *SEA* have been combined to a single spectrum composed of multiple JONSWAP spectra, and the presented significant wave heights and peak wave periods are derived from the integrated spectrum. The results are stochastic both with respect to the choices of

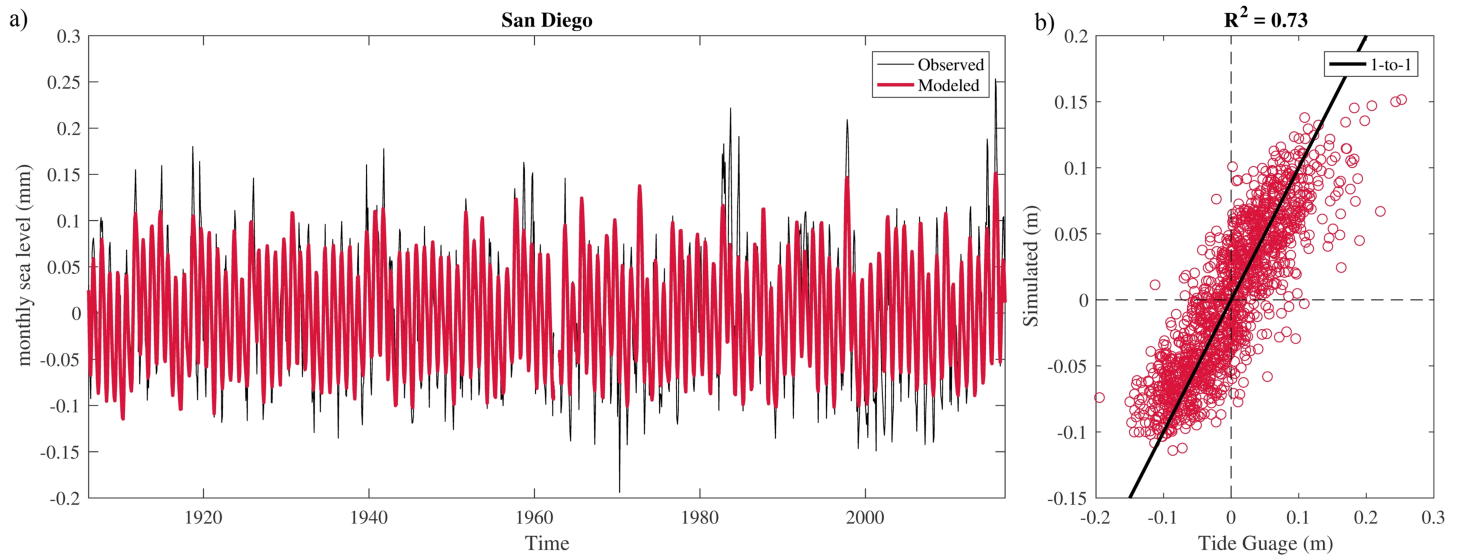


Figure 7. (a) MMSLA observed at the San Diego tide gauge since 1908 (black), with the predicted water level provided by a regression model of $APC_1(t)$, $APC_2(t)$, and $APC_3(t)$ (red). (b) A 1-to-1 comparison of regression predicted water level and the observed.

synoptic DWT patterns by the ALR model and the random picks from the Bernoulli sea state distributions and subsequent copulas of environmental conditions.

Although various metrics with respect to the climate emulator have been validated in earlier sections and in Appendix A, the final validation of the methodology necessitates comparison of the TWL observations from section 2 to the emulator output. In Figure 9, 100 synthetic 39-year simulations are compared to the historical distributions via quantile-quantile plots. The one-to-one line in the qq-plots is captured by the envelope for each of the individual parameters, indicating that the historical record is reproduced despite the simulated distributions being a combination of 42 separate wave and surge clusters (DWTs). Recovering the input distributions is also dependent on numerous other steps in the model, such as quality Gaussian copula correlations and realistic occurrence probabilities of each DWT. The tails of each component are more variable due to the intentional use of GEVs (for wave height and storm surge distributions), which allows for some synthetic simulations to contain more extremes.

Synthetic simulations were generated using 500-year chronologies of ENSO and MJO as input to the emulator, providing hypothetical chronologies containing new combinations of TWL components and empirical estimates of extreme TWL events using the count back method (Hawkes et al., 2002). Confidence in emulator output is further provided by comparing predicted extremes from traditional methods (Coles, 2001) to extremes obtained during 100 synthetic simulations (Figure 10a). Recurrence events with <1% probability derived from each synthetic simulation (red dots) mostly fall within 95% confidence intervals obtained by 1000 bootstraps (Efron & Tibshirani, 1986). The benefit of the presented methodology is that each extreme in the simulation is associated with its individual TWL components and the causal climate state. As noted in Figure 10a, the two most extreme TWLs both occurred during El Niño winters, motivating the need to better understand extremes conditioned on this climate state. Traditional extrapolation using only a few historical El Niño observations would have little confidence, but TESLA can directly simulate the extreme tails of conditional distributions with respect to climate. After 1000 TESLA simulations, annual maximum return during El Niño and La Niña AWTs was isolated to reveal a consistent 20–25 cm higher water level at all return periods during El Niño years (Figure 10b). Variability in the return period was assessed by separating the >7,000 years within each AWT into 100-year blocks and utilizing the count-back method. The more extreme events contain greater variability and greater overlap between the two climate states due to an increasing relative contribution from wave run-up. The other four AWTs are not presented in Figure 10b, but the means of their 100-year blocks all fall between the El Niño and La Niña extremes.

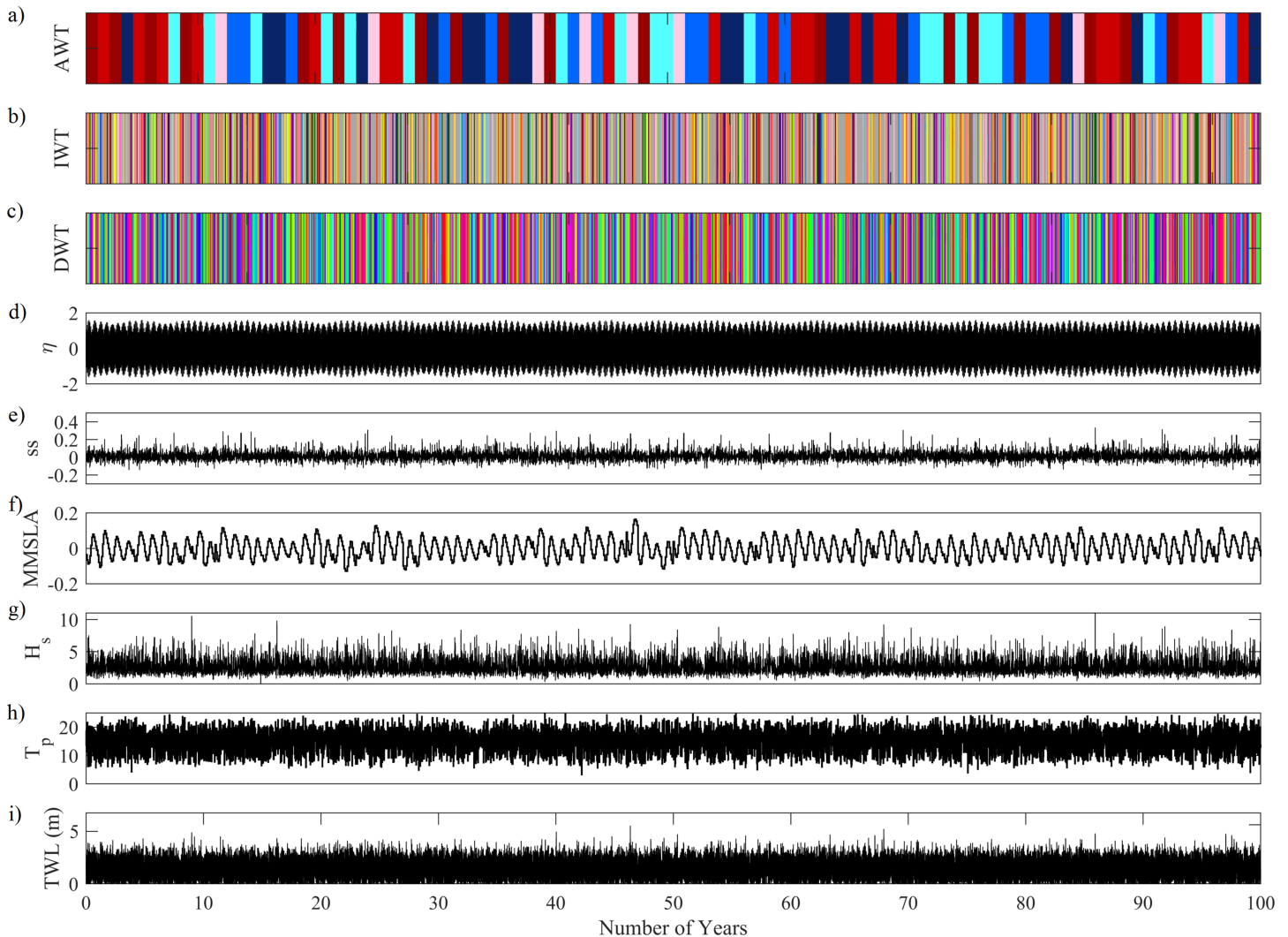


Figure 8. (a) 100 years of synthetic AWT chronologies with color of the bar synonymous with Figure A1. (b) Daily synthetic IWT chronologies with color of the bar synonymous with Figure A3. (c) Daily DWT output generated by the ALR model resulting from (a) and (b) as inputs. Color of the bars is synonymous with Figure 3. (d) deterministic tide derived from T_Tide toolbox in meters and relative to mean sea level. (e) storm surge in meters sampled from copulas. (f) MMSLA defined by a regression of the AWT's PCs. (g) significant wave height derived from a combined directional spectrum composed of NH, SH, and SEA waves. (h) peak period from the combined wave spectrum. (i) the resultant compound TWL as defined by equation (1).

The direct simulation of extreme compound TWL events also allows for a greater investigation of the respective constitutive components. Similar to the findings of Serafin et al. (2017), Figure 11 demonstrates how annual maxima can occur across a broad range of values within each TWL component. Identifying the 1% recurrence events (red dots in Figure 11, defined as the fifth largest event in each simulation) reveals the degree to which this variability is retained in extreme events. The results suggest that annual events can be either wave or SWL dominated, but that the joint dependence between components becomes progressively more important at longer return periods. While most of the 1% recurrence events occur when wave heights are greater than 5 m and wave periods longer than 15 s, there is an infinite combination of univariate drivers that can combine to generate compound extreme events—even for a simple TWL proxy such as equation (3). Such different TWL components can lead to different impacts on the open beach (Cohn et al., 2019; Serafin et al., 2017; Serafin et al., 2019) and different flood extents in the backshore (Bilskie & Hagen, 2018). The presented framework can be a tool used to make informed decisions for the input conditions to dynamical numerical modeling studies assessing flood extents and hazard zones contingent on future extremes (Barnard et al., 2019; Erikson et al., 2018).

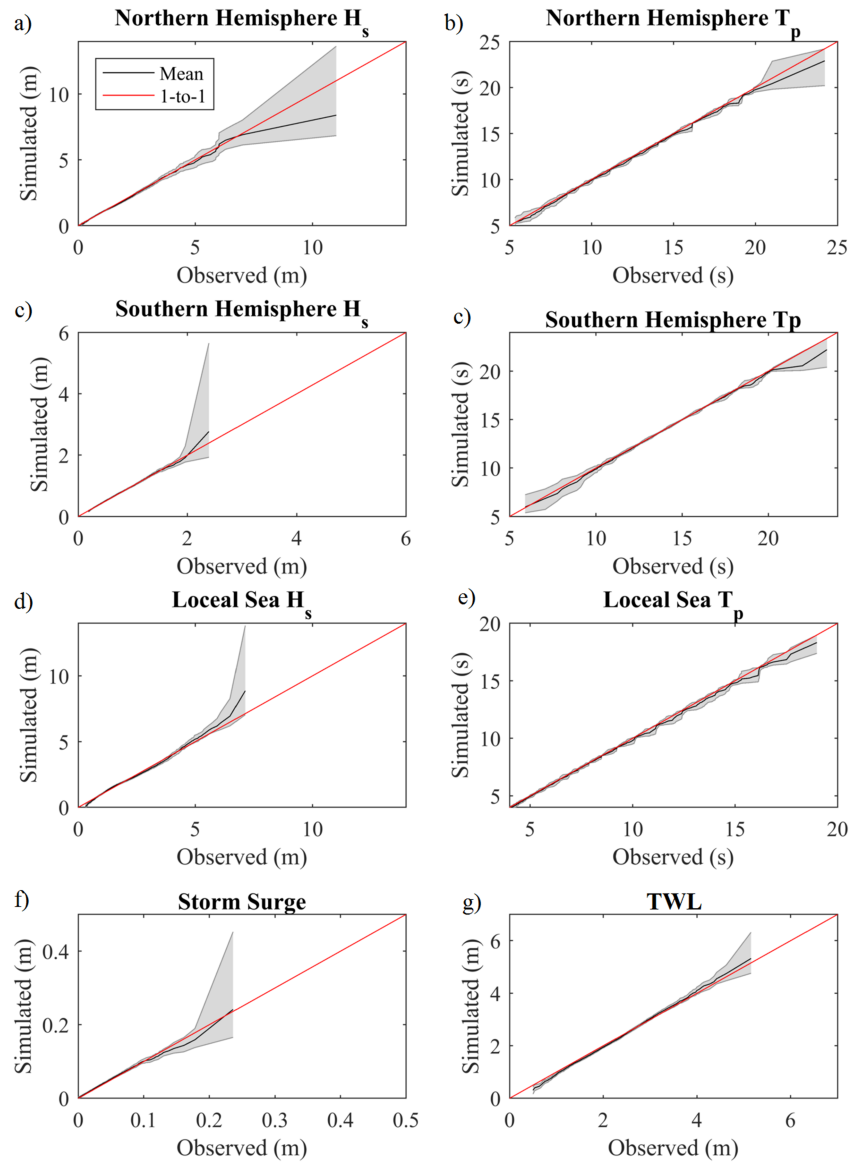


Figure 9. Quantile-quantile plots comparing 39 years of historical observations to 100 synthetic 39-year simulations of (a) *NH H_s*, (b) *NH T_p*, (c) *SH H_s*, (d) *SH T_p*, (e) *SEA H_s*, (f) *SEA T_p*, (g) *SS*, and (h) *TWL*. Envelopes of variability are colored gray and the mean across all simulations is the black line.

Figure 12 presents the probability of the annual maxima and 100-year return level events occurring during each DWT (same grid as Figure 3). Figure 12b reveals which synoptic weather patterns San Diego is particularly sensitive to, highlighting several patterns containing large north Pacific low-pressure systems. Such weather patterns are typically indicative of a dip in the jet stream and a steering of winter storms toward California. Expressing the same 100-year events with respect to the AWTs further highlights the importance of considering the interannual climate (Figure 12d). El Niño years are the least common AWT in the total record, and yet account for almost 40% of 100-year events simulated in this work.

The conditional probabilities with respect to climate phenomena could be useful for future studies considering climate change and shifts in weather patterns. Although the presented framework is dependent on a stationary assumption of climate (i.e., weather pattern probabilities of occurrence during the 39 years of CFSR data are consistent within simulations), the extension of the stochastic climate emulator to future emission scenarios is feasible with GCM output. GCMs utilize the same fundamental SLP and SST fields as the emulator, and previous studies have developed techniques for identifying changing occurrence

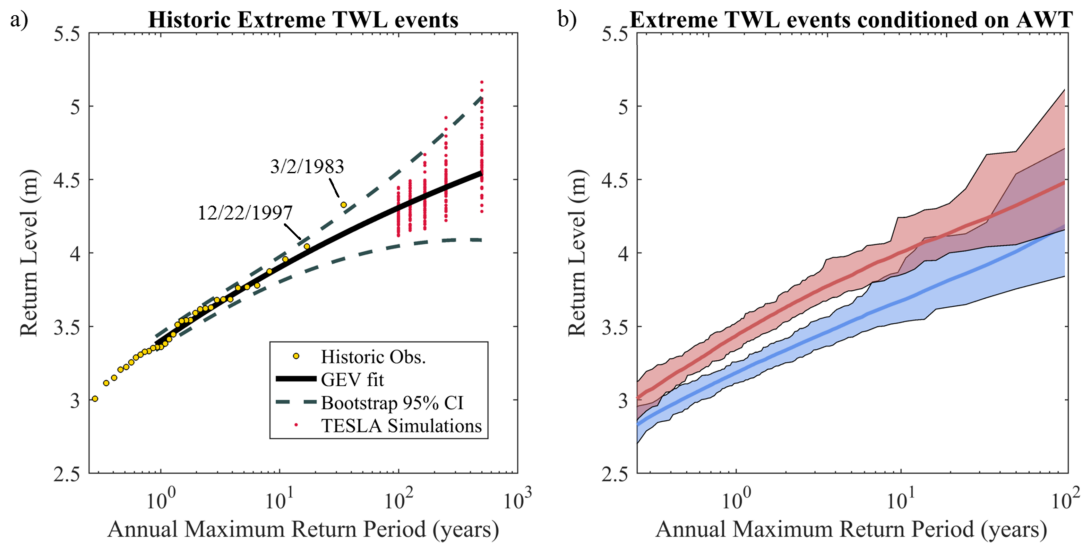


Figure 10. (a) Return periods of annual maxima for the top 5 TWL events from 100 different 500-year TESLA simulations (red dots ordered by count-back method) compared to historic annual maxima (blue dots) and associated GEV extrapolations (black line) and uncertainty bounds by both the delta method (gray dotted lines) and bootstrapping (gold dotted lines). (b) Annual maxima return periods specific to El Niño years (red) and La Niña years (blue) derived from 10,000 synthetic years of climate and associated TWLs. Bold lines represent the mean across 100-year blocks with shading representative of the maximum and minimum TWLs simulated at each return period.

probabilities between historical and GCM output (Perez et al., 2015). The change in synoptic weather pattern probabilities, or of SSTA El Niño activity (e.g. Cai et al., 2014), could be included in the covariates of the ALR model and would downscale to changes in the sea-state probabilities and ultimately generate different TWL component distributions and extremes. This is a natural next step for employing the emulator to assess future flooding under nonstationary climate change and sea-level rise.

5. Discussion

The emulator presented in this study combines multiple methodologies into a single framework. Each step has sensitivities and limitations, which are addressed within the discussion, as well as the broader applicability of the methodology to other study sites.

5.1. Sensitivities

Although multiple user decisions are built into the framework, automated tests for statistical significance can aid in most decisions (i.e., whether a GEV or an empirical distribution should be fit to a subset of data or how many empirical orthogonal functions (EOFs) to use in creating climate indices). In the first step of the methodology, an a priori user decision must be made regarding the number of clusters used to create each of the climate indices. The purpose of the clusters is to separate climate variability and associated sea-state variability. Increasing the number of clusters not only identifies greater sea-state variability but also results in a trade-off due to less data contained within each cluster, which can lead to poorly defined marginal distributions and associated correlations. This problem is a function of the length of the observation record of sea-state parameters as opposed to a shortcoming of the ALR approach to simulating weather chronologies. Two additional DWT configurations fit with the ALR model of AWT, IWT, and seasonality with 55 clusters and 70 clusters both returned high skill between historical and mean simulated probabilities (R correlation values of 0.94 and 0.93, respectively). All AWT PCs and MJO PCs retained significance in the two alternate ALR model configurations, suggesting the fundamental linkage of large-scale climate to a local tailor-made atmospheric predictor is a technique insensitive to the specific number of weather types used in analysis.

The use of Markov chains to generate 1,000s of years of large-scale climate weather types introduces uncertainty on the order of ~2–3% change in the probability of transitioning from one WT to another WT

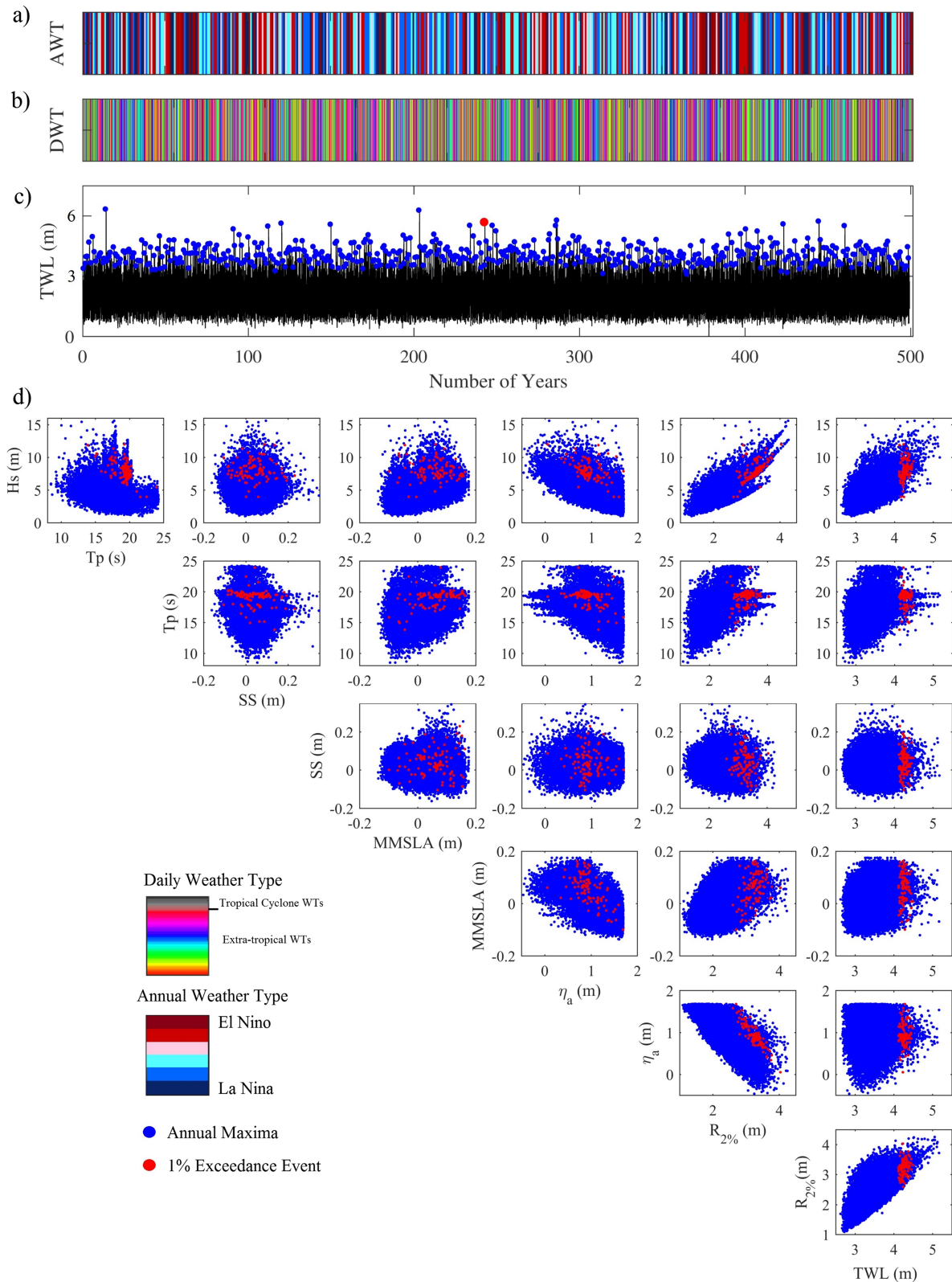


Figure 11. A 500-year simulation of (a) AWTs and the derived (b) DWTs with the ALR model. Hydrograph peaks expressed as (c) TWLs composed of all still water level plus run-up. Blue dots in (c) signify the annual maxima in the 500-year record, and the red-dot denotes the 5th largest event (the 1% recurrence event equivalent). Bottom scatter plots show the variability in annual maxima (blue dots) across 100 500-year simulations (50,000 years in total) and red dots are the 100 1% recurrence events in those simulations.

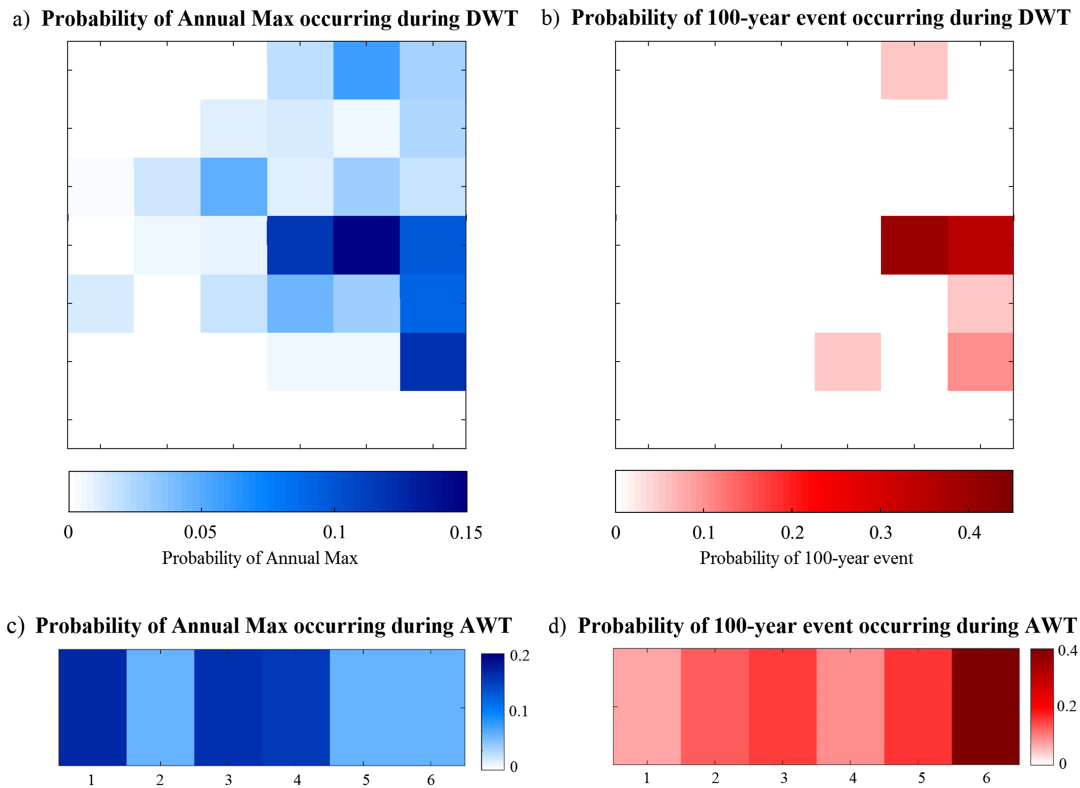


Figure 12. The occurrence probability of (a) annual maxima TWL events and (b) 100-year events occurring within a specific DWT (weather pattern location consistent with Figure 3). The same (c) annual maxima and (d) 1% recurrence events expressed as probability of occurrence within AWTs. AWT numbering and layout consistent with Figures 3 and A1.

(see Appendices A2 and A3). This affects the sequencing within the synthetic time series and thus a metric assessing the slowly varying time-dependent extremes may be sensitive to such large-scale sequencing. The synthetic climate sequences are also dependent on the order of the Markov chain used, which in turn exhibits dependencies on the length of time in the training dataset. This was one of the main considerations in developing the AWT Markov chain with data from 1880 to 2018 rather than higher resolution products available in the satellite era that provided fewer transitions to train the Markov and resulted in greater variability in synthetic time series.

In terms of simulated TWL parameters, the decision to use only the maximum TWL during a hydrograph was made to reduce complexity by focusing on joint extremes, but also leads to neglecting extremes of individual parameters if they were not co-occurring with the TWL maxima. The component most affected by the hydrograph methodology was *SH* wave characteristics; however, its reduced relevance to historical TWL maximas relative to *NH* and local *SEA* contributions was preserved by the presented methods. The application of Gaussian copulas for joint probabilities was another user decision applied after initial random sampling from each univariate distribution resulted in underestimation of the extremes. This element of the methodology could be improved in the future with an automated goodness-of-fit decision choosing which of the many copula formulations best defines the joint probabilities.

5.2. Limitations

This paper provides a methodology for incorporating climate states into synthetic coastal condition models and demonstrates how such dependencies on climate states may be useful for studies projecting exposure to coastal hazards in the changing 21st century climate. However, the applied methods incorporate several simplifying assumptions to efficiently derive a univariate TWL, including the assumption of an average beach slope being representative, the use of an empirical equation for $R_{2\%}$, and the use of linear superposition of water level components. Local forcing is not dynamically downscaled to specific locations, which

inherently neglects nonlinear interactions between surges and tides while also missing the alongshore variability of the hazard resulting from wave propagation over local bathymetry. This is a common problem associated with generating 1,000s of years of conditions, which would necessitate considerable computation resources to dynamically downscale. Recent developments in hybrid meta-models, or surrogate models, provide a promising compromise between process-based downscaling and efficiency (Bass & Bedient, 2018; Del-Rosal-Salido et al., 2019; Parker et al., 2019), which could allow for statistical studies such as this to derive transect-specific process-based results.

5.3. Future Applications

The majority of the methods presented in this framework are transferable to any new location via automated approaches, despite all of the results and the atmospheric predictor being tailor-made for San Diego. However, applying this exact framework to locations far from the equatorial Pacific Ocean or regions where ENSO is not the dominant driver of interannual variability, potentially requires different AWTs to drive the ALR model. Although a tailor-made ENSO index was developed in this study, the covariates provided to the ALR model could be readily replaced with traditional climate indices similar to how this study utilized a common MJO index product provided by meteorology agencies. In this sense, the techniques and philosophy of correlating large-scale climate variables with local TWL components are transferable. Once large-scale climate drivers are properly defined, and dependencies across timescales are confirmed to be significant, the framework's computational time is relatively short. Thousands of years of chronological sea-states can be produced on the order of hours compared to the months to years that dynamically running a climate model and subsequent wave/surge model would require. A repository of codes relevant to each of the methods considered in this study is provided at <https://github.com/teslakit/teslakit>, as well as Jupyter notebooks demonstrating application to other sites in the Pacific Ocean.

6. Summary

The Time-varying Emulator for Short- and Long-Term Analysis of coastal flood hazard potential is presented as a methodology for producing robust estimates of coastal flooding risk while accounting for the dependencies of local TWL components on the fundamental drivers of large-scale climate. The model accounts for annual external energy input from the sun (seasonality), persistent energy storage in the earth system (SSTAs representing ocean heat content and ENSO variability), reflected energy emitted back to space (the outgoing longwave radiation composing the MJO Index), and energy dissipation in the form of spatially and temporally varying synoptic weather patterns. The emulator additionally quantifies the joint probabilities for TWL components contributing to coastal sea level variability to explore the full dimensionality of extreme flooding resulting from compound events.

The framework demonstrates the potential for weather typing and auto-logistic regression as methods to reduce complexity (dimensionality) of the climate system and simulate dependence across multiple timescales and processes. The initial input to the emulator is spatial climate patterns, which results in an explicit link between climate forcing patterns and TWL variability and identifies which climate and weather patterns San Diego is particularly sensitive to from an extreme perspective. The output additionally includes the full dimensionality of extreme compound events, revealing the infinite number of multivariate combinations that create compound TWL flooding.

TESLA-flood is a computationally efficient tool with the potential to identify the composition of extreme coastal flooding events of the future. The input predictors to the emulator are effectively the output variables produced by GCMs, which means frameworks such as TESLA-flood have the potential to statistically downscale large-scale climate predictions to local coastal hazard assessments in the Pacific Ocean. Such assessments are increasingly being performed with high fidelity hydrodynamic and wave models capable of defining realistic flood extents of historic events (e.g., Barnard et al., 2019). TESLA-flood's output can be used as the boundary conditions for these deterministic models, providing a link between state-of-the-art climate science and state-of-the-art coastal hydrodynamic models for the improvement of future hazard assessments.

Appendix

A.1. Weather-Type Classifications and Chronology

Climatologists have widely accepted classification methodologies that decompose time-varying spatial datasets into a certain number of representative climatic states or patterns as flexible frameworks for assessing the nonlinear nature of asymmetrical oscillating phenomena (Huth et al., 2008; Philipp et al., 2016). A wide range of automated techniques exist (i.e., leader algorithms, optimized partitioning, etc.), and the resultant patterns can be dependent on the technique employed. A tailor-made climate index was developed for this study, largely due to a desire to preserve nonlinearity in the climate system and retain more information than off-the-shelf univariate indices provide (Williams & Patricola, 2018). The technique employed is a WT-based framework which has been used to explore climate variability in many of the physical processes relevant to coastal erosion and flooding extremes (e.g., Camus et al., 2014). The weather types in this work are obtained through a two-step process of identifying dominant modes of spatial variability through EOFs and subsequent K-means clustering with respect to the temporal amplitude of each PCs (Gutierrez et al., 2013). The resulting centroids for each cluster thus have an amplitude associated with each EOF and can be remapped to a spatial weather type considered to be representative of all instances associated with that centroid. Weather-typing was performed to identify representative states of ENSO (Appendix A.1.), MJO (Appendix A.2.), and representative daily atmospheric circulation patterns (Appendix A.3.).

A.2. Classifying the El Niño Southern Oscillation

Typical ENSO indices monitor SST data from a region in the equatorial Pacific Ocean as a means of tracking where anomalously warm water is located (i.e., the Oceanic Niño Index and the NINO3.4 Index). Average monthly SST anomalies (SSTA) were extracted from the Extended Reconstructed Sea Surface Temperature v4 (ERSSTv4; Huang et al., 2015) for a rectangular region from 120°E to 280°E and 5°N to 5°S at a resolution of 2.5°. Anomalies were computed by removing 11-year running averages for each month at every node. The monthly longitudinal location of anomalously warm water and its temporal behavior during the year was preserved in the development of AWTs by averaging monthly SSTA values at each longitude to construct Hovmöller diagrams (Figure A1, Hovmöller, 1949). Each diagram begins in June and ends in the following May to capture SSTA variability throughout the boreal winter. Weather typing of Hovmöller space (e.g., K-means clustering of three dominant PCs from EOF analysis) was used to identify predominant spatial modes and associated temporal behavior. EOF₁ explains 48% of the variance, predominantly related to the seesaw effect of warm water anomalies located either east or west of 165°E. The yearly PC values of EOF₁ strongly correlate with the average annual Oceanic Niño Index ($R^2 = 0.94$) and average annual NINO3.4 ($R^2 = 0.91$) indices, indicating that the PCA of Hovmöller space captures the same dominant interannual variability identified by classical ENSO indices. EOF₂ (11% of the variance) is predominantly associated with shifting seasonal anomalies in the east Pacific, while EOF₃ (8% of the variance) exhibits a temporal and spatial pattern akin to a Kelvin wave of an SSTA propagating west to east during NH summer and fall. The annual PCs of EOF₁, EOF₂, and EOF₃ are henceforth referred to APC₁, APC₂, and APC₃ respectively (Figure A1a–A1c).

The K-means clustering of APC₁, APC₂, and APC₃ accounts for 19% more variance than classical ENSO indices based solely upon the leading EOF (Figure A1d). Remapping the representative centroids of each cluster back to Hovmöller space reveals the multiple flavors of ENSO (Figure A1f). Annual weather type #6 (AWT#6) clusters years of positive SSTA in the east Pacific, which are representative of canonical El Niño years and includes the classic examples of 1982–83, 1997–98, and 2015–16 (Figure A1b). AWT#5 clusters Modoki El Niño years, with the largest anomalies slightly further west along the equator than AWT#6, and identifies such Modoki years as 1994–95, 2002–03, and 2009–10 (Ashok et al., 2007). The opposite end of the spectrum is AWT#1, which exhibits negative SSTA in the east Pacific representative of La Niña years. Other ENSO states identified by the clustering method are interpreted as transition years between the El Niño/La Niña extremes. AWT#4 identifies increasing positive SSTA throughout the year and often occurred prior to El Niño, while AWT#3 exhibits the opposite SSTA behavior and is a precursor to La Niña.

The designation of six AWTs was a subjective decision weighing how many clusters were necessary to reproduce classical ENSO patterns identified in the literature while creating clusters with enough data points to

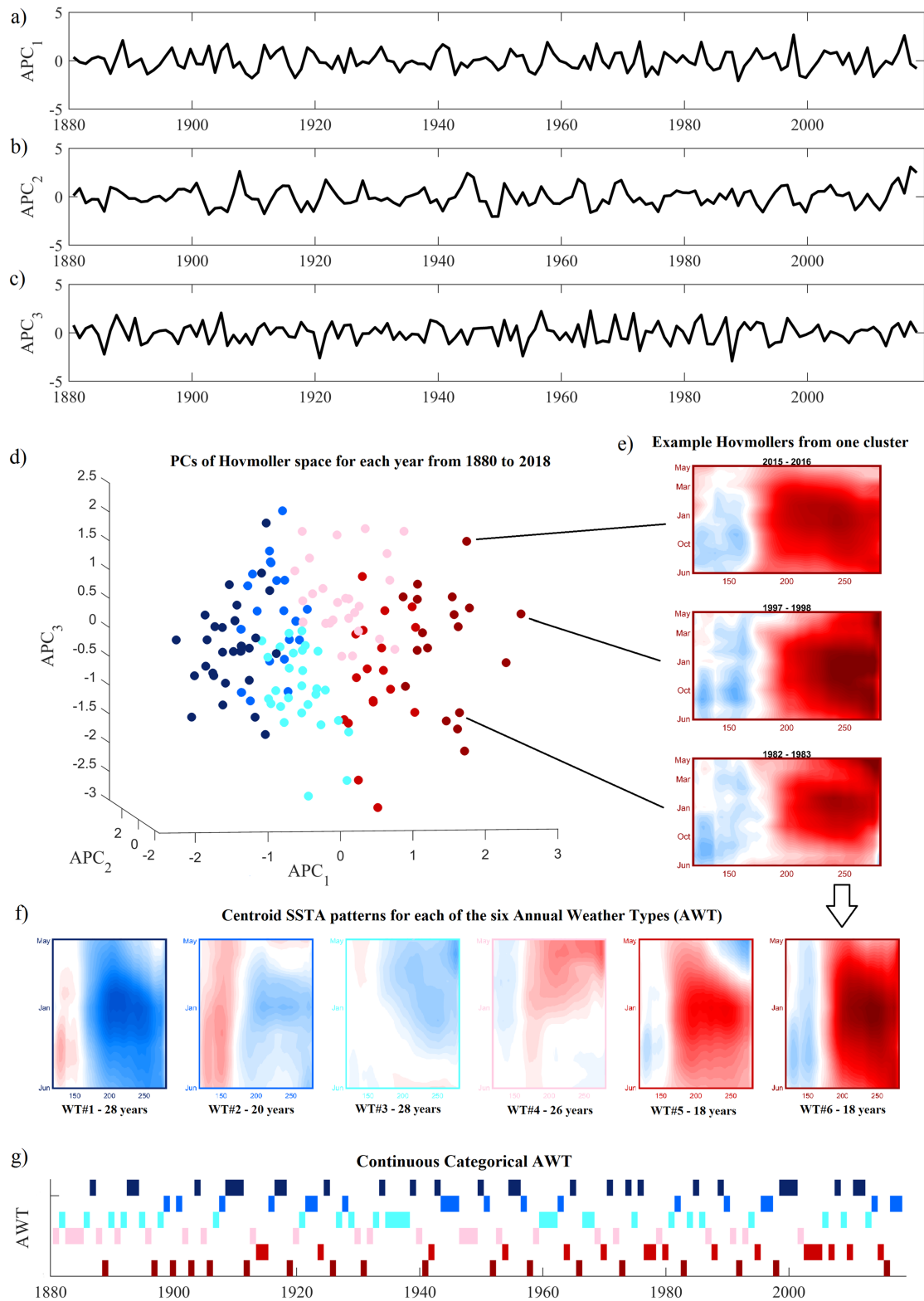


Figure A1. The weather-typing process as a method for converting temporally continuous PCs into AWTs. (a–c) The temporal PCs associated with the leading three EOF patterns of SSTA variability for each year from 1880 to 2018, which are projected into PC-space in (d). Color of the points denotes years identified as belonging to the same cluster by K-means. (e) Example Hovmöller diagrams for three El Niño years all belonging to the same cluster. (f) The six representative SSTA patterns defined by the centroid of their cluster and outlined by the same color as the points in (d) which contribute to defining their centroid. (g) Redefining all years by their respective AWT, with color denoting the corresponding cluster in (f).

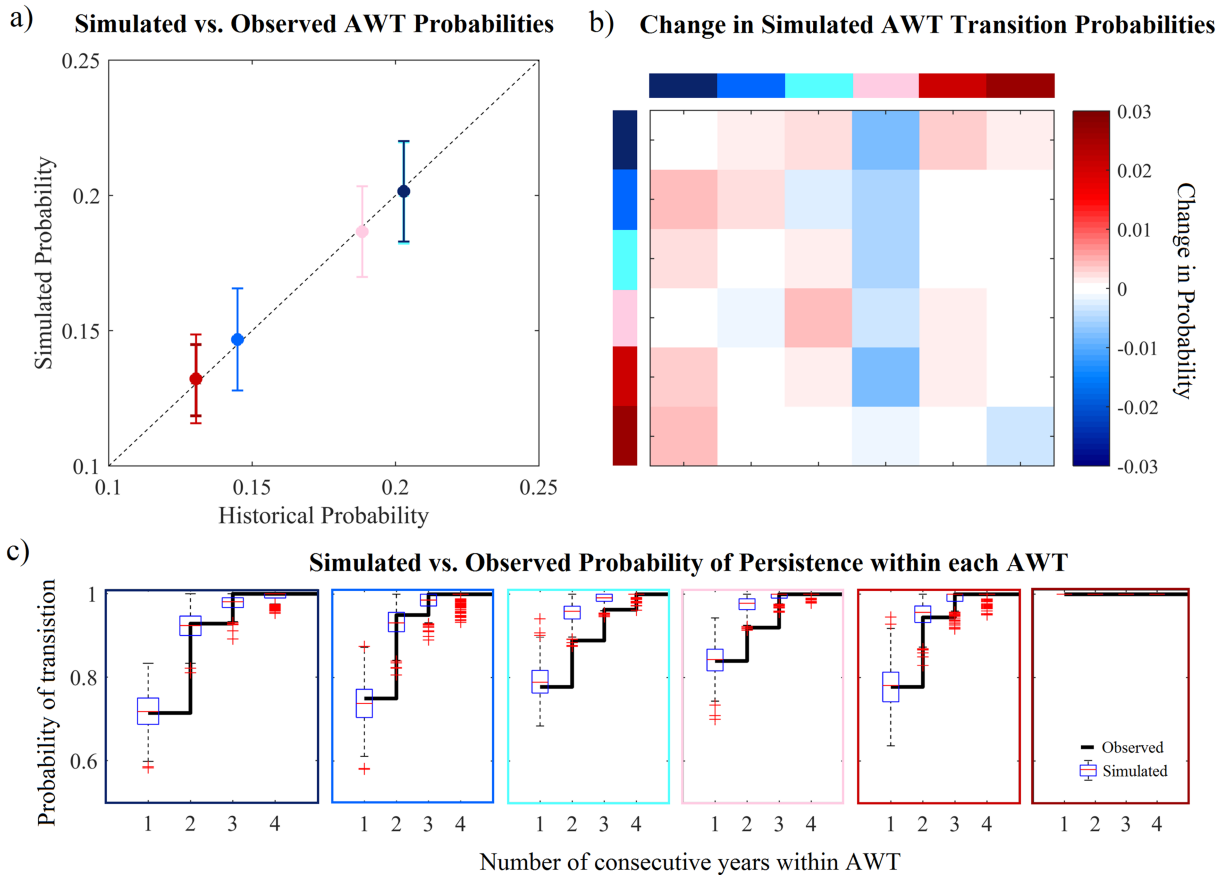


Figure A2. Comparison of multiple probabilistic and chronological characteristics for simulated and observed AWT time series. (a) The historically observed probability directly compared to the average across 100 simulations and the standard deviation about that averaged (whiskers). (b) The change between the observed Markov transition matrix and the simulated time series. The diagonal is the change in probability of remaining within the same AWT for multiple years, while the columns in each row are the change of probability in transitioning to each of the other AWTs. (c) The persistence of each AWT is assessed by the probability of transition or the likelihood of switching to a different AWT in the following year. Observed likelihoods in black and the box plots denote the average, standard deviations, and outliers across 100 simulations. Colors in (a), (b), and (c) align with the outlined colors of the AWTs provided in Figure 3.

simulate temporal evolution of synthetic records of AWTs. The chronological sequencing of AWTs was found significant to a second-order Markov chain, and simulated synthetic time series from the Markov chain reproduced not only the total probability and transition probabilities but also the average occurrence interval and persistence of each ENSO state (Figure A2). Synthetic categorical AWTs were then converted to PC space by defining tri-variate Gaussian copulas (e.g., Masina et al., 2015; Wahl et al., 2012) for each AWT using the marginal distributions of its respective three PC components APC_1 , APC_2 , and APC_3 . Each simulated categorical ENSO is thus defined by a random number generator converted to a triplet of APC_1 , APC_2 , and APC_3 from the appropriate copula, effectively providing synthetic AWT time series with the potential to not only produce new chronologies but also new SSTA behavior (i.e., create El Niño and La Niña events statistically consistent with observations but not exact replicas of the limited number of historical observations).

A.3. Clustering the Madden-Julian Oscillation

The intensity and geographic location of MJO convection are commonly identified by the MJO index based on the first two EOFs of equatorially averaged outgoing longwave radiation and 850- and 200-hPa zonal winds (Wheeler & Hendon, 2004). The temporal PCs associated with the same two EOFs contributing to the MJO index are used in this study, with daily values available since 1975. It is a common practice in the MJO literature to separate the longitudinal location of the center of convection into eight longitudinal phases (Wheeler & Hendon, 2004). This convention was preserved in a daily index in this study, intended

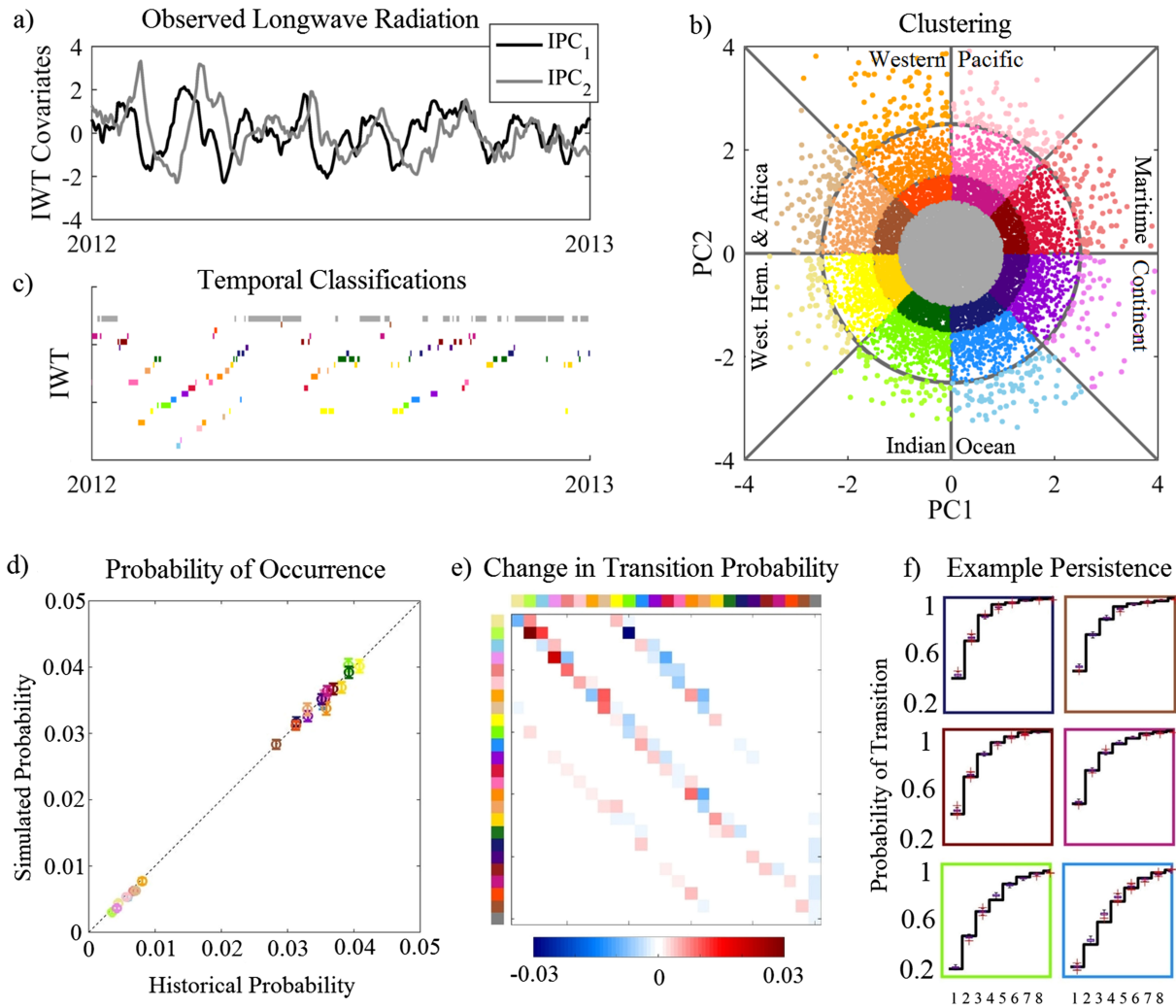


Figure A3. (a) An example of the temporal variability in IPC_1 and IPC_2 of outgoing longwave radiation. (b) Demonstration of clustering with IPC_1 and IPC_2 for global location and strength of MJO convection. (c) The time period from (a) shown by classification color determined by clustering in (b). (d) The historically observed probability directly compared to the average across 100 Markov simulations and the standard deviation about that averaged (whiskers). (e) The change between the observed Markov transition matrix and the simulated transition probabilities. (f) The persistence of 6 example IWTs assessed by the probability of transition, or the likelihood of switching to a different IWT in the following day. Observed likelihoods in black and the box plots denote the average, standard deviations, and outliers across 100 simulations. Colors in (d), (e), and (f) align with the colored clusters denoted in (b).

to be a proxy for intra-seasonal MJO oscillations by clustering the two leading PCs (henceforth referred to as IPC_1 and IPC_2) of outgoing longwave radiation into eight pre-defined longitudinal phases and further separating into three categories of low, medium, and high convection strength (analogous to conventions in Laflour et al., 2015; Figure A3). A separate cluster was created for times when the location of the MJO is considered to have low certainty (when the vector magnitude of PC1 and PC2 is less than 1, Wheeler & Hendon, 2004). Altogether, the 25 clusters of IWTs effectively create categorical MJO states analogous to the AWT states described above, while preserving the ability to compare results to other studies investigating MJO teleconnections to ENSO (Henderson & Maloney, 2018) and MJO relationships to waves and water levels (Marshall et al., 2015).

Synthetic time series of the MJO are obtained with a Markov chain of the predefined IWT categorical states (statistically significant to the third order) and subsequent sampling from joint distributions of IPC_1 and IPC_2 within each cluster identified in Figure A3. A lagged correlation between spring and summertime MJO activity and autumn and wintertime NINO3.4 index was found during the 1990s but was not

statistically significant in the 1980s and 2000s (Tang & Yu, 2008), and the probabilities and persistence of the categorical IWT states derived in this study were found to be independent of our AWTs. This suggests that the two climate processes can be simulated as individual phenomena operating at separate time scales. When consecutive days in the synthetic record are sampled from the same categorical state, the randomly picked EOF pairs are ordered to preserve counterclockwise propagation of the MJO around the globe in a consistent direction. Transition probabilities and persistence within a particular IWT state are provided in Figure A3, where changes in probability between the historical and synthetic time-series are less than 2% and greatest change in the Markov matrix are observed in the much less frequent IWT states.

A.4. Clustering Synoptic Weather

Weather is represented by SLP fields and the squared gradients (SLPG) of those fields obtained from the CFSR (Saha et al., 2011). SLP fields effectively capture high- and low-pressure systems while SLPG are related to the strength of the wind stress generating waves and wind induced storm surge. Only the SLPs and SLPGs in a region considered to influence San Diego were included in the analysis; however, the size of the region extends to include distant weather systems due to the generation of swell, which propagates across the ocean and affects the local wave run-up. The region of influence was defined using the Evaluation of Source and Travel-time of wave Energy reaching a Local Area (ESTELA) method (see energies in Figure 1a; Perez et al., 2014), which identifies the relevant amount of energy directed along great circle arcs toward the study site using full directional wave spectra in the global IFREMER wave hindcast (Rasclé & Ardhuin, 2013).

The SLP and SLPG fields were further modified to consider the travel time of swell waves, which arrive to the study site on the order of days to weeks after generation by a distant weather system. An atmospheric predictor, $P_{t,x,y}$, was created dependent on the isochrones of average wave travel time identified by ESTELA:

$$P_{t,x,y} = \{ \dots, SLP_{t-i,\Omega_i}, SLP_{t-i,\Omega_i}, \dots \} \quad \text{for } i = 1, \dots, p \quad (4)$$

where Ω_i represents the spatial domain between isochrones $i - 1$ and i , and p is the number of isochrones of the furthest wave generation region (Hegermiller et al., 2017).

Weather-typing of $P_{t,x,y}$ was performed at a daily time scale to create a daily weather type (DWT) as a proxy for synoptic SLP patterns (Camus et al., 2014). The number of clusters in this analysis was set at 36, and the K-means was performed iteratively until every cluster contained at least 100 days (sensitivity to these decisions is discussed in section 5). Remapping the centroids of each cluster from PC space to SLP space results in the top 6 rows of DWTs in Figure 3a. Six additional DWTs were created to represent eastern Pacific tropical depressions and TC categories 1 through 5 by removing days with TC generation from the initial $P_{t,x,y}$ dataset prior to K-means clustering (bottom most row in Figure 5a; TC generation defined by the HURDAT2 database, Landsea & Franklin, 2013). Separating the TCs as explicit categorical variables ensured that the probabilities of occurrence and conditional dependencies of the rare events were persevered in the framework rather than being clustered into extra-tropical synoptic circulation patterns as the most distance points from a prescribed centroid.

Acronyms and Abbreviations

AWT	Annual Weather Type
DWT	Daily Weather Type
ENSO	El Nino Southern Oscillation
EOF	Empirical orthogonal function
EVA	Extreme value analysis
GCM	General circulation model
GEV	Generalized extreme value function
IWT	Intraseasonal Weather Type
MJO	Madden-Julian Oscillation
MMSLA	Monthly mean sea level anomaly

NH Northern hemisphere waves
 PCA Principal component analysis
 SEA Locally generated wind waves
 SH Southern hemisphere waves
 SLR Sea level rise
 TC Tropical cyclone
 TWL Total water levels

Acknowledgments

A repository of codes relevant to each of the methods considered in this study is provided at <https://github.com/teslakit/teslakit>. The NCEP Climate Forecast System Reanalysis (CFSR) and Extended Reconstructed Sea Surface Temperature Version 4 (ERSSTv4) data are freely available through NOAA/NCAR, Boulder, Colorado, USA, from their website at <https://rda.ucar.edu/datasets>. Madden-Julian Oscillation EOFs were downloaded from the Australian Bureau of Meteorology at www.bom.gov.au/climate/mjo. The authors thank Melisa Menendez for sharing GOW2 hindcast data for Southern California, and Katherine Serafin for splitting the San Diego tide gage signal into its constitutive components. The authors also sincerely appreciate the contributions of three anonymous reviewers during the review process. This work would not have been possible without funding from the Strategic Environmental Research and Development Program's grant DOD/SERDP RC-2644. AR, LC, and FJM acknowledge the partial fund of the project by the regional government of Cantabria entitled "SISTEMA INTEGRADO DE PREDICCIÓN PROBABILÍSTICA DE INUNDACIÓN Y EROSION EN PLAYAS (SODERCAN/FEDER)". J.A.A. Antolínez is indebted to the MEC (Ministerio de Educación, Cultura y Deporte, Spain) for the funding provided in the FPU (Formación del Profesorado Universitario) studentship (BOE-A-2013-12235).

References

- Albert, S., Leon, J. X., Grinham, A. R., Church, J. A., Gibbes, B. R., & Woodroffe, C. D. (2016). Interactions between sea level rise and wave exposure on reef island dynamics in the Solomon Islands. *Environmental Research Letters*, *11*. <https://doi.org/10.1088/1748-9326/11/5/054011>
- Antolínez, J. A. A., Méndez, F. J., Camus, P., Vitousek, S., Gonzalez, E. M., Ruggiero, P., & Barnard, P. (2015). A multi-scale climate emulator for long-term morphodynamics (MUSCLE-morpho). *Journal of Geophysical Research, Oceans*, *121*. <https://doi.org/10.1002/2015JC011107>
- Ashok, K., Behera, S. K., Rao, S. A., Weng, H., & Yamagata, T. (2007). El Niño Modoki and its possible teleconnections. *Journal of Geophysical Research, Oceans*, *112*(11), 1–27. <https://doi.org/10.1029/2006JC003798>
- Barnard, P., Erikson, L. H., Foxgrover, A. C., Finzi Hart, J. A., Limber, P., O'Neill, A. C., et al. (2019). Dynamic flood modeling essential to assess the coastal impacts of climate change. *Scientific Reports*, *9*(1), 4309. <https://doi.org/10.1038/s41598-019-40742-z>
- Barnard, P. L., Hoover, D., Hubbard, D. M., Snyder, A., Ludka, B. C., Allan, J., et al. (2017). Extreme oceanographic forcing and coastal response due to the 2015-2016 El Niño. *Nature Communications*, *8*(1), 1–8. <https://doi.org/10.1038/ncomms14365>
- Barnard, P. L., Short, A. D., Harley, M. D., Splinter, K. D., Vitousek, S., Turner, I. L., et al. (2015). Coastal vulnerability across the Pacific dominated by El Niño/Southern Oscillation. *Nature Geoscience*. <https://doi.org/10.1038/ngeo2539>
- Bass, B., & Bedient, P. (2018). Surrogate modeling of joint flood risk across coastal wetlands. *Journal of Hydrology*, *558*, 159–173. <https://doi.org/10.1016/j.jhydrol.2018.01.014>
- Beckley, B. D., Callahan, P. S., Hancock, D. W., Mitchum, G. T., & Ray, R. D. (2017). On the “Cal-Mode” Correction to TOPEX satellite altimetry and its effect on the global mean sea level time series. *Journal of Geophysical Research, Oceans*, *122*, 8371–8383. <https://doi.org/10.1002/2017JC013090>
- Bilskie, M., & Hagen, S. (2018). Defining flood zone transitions in low-gradient coastal regions. *Geophysical Research Letters*. <https://doi.org/10.1002/2018GL077524>
- Cai, W., Borlace, S., Lengaigne, M., van Rensch, P., Collins, M., Vecchi, G., et al. (2014). Increasing frequency of extreme El Niño events due to greenhouse warming. *Nature Climate Change*, *4*, 111–116. <https://doi.org/10.1038/nclimate2100>
- Callaghan, D. P., Nielsen, P., Short, A., & Ranasinghe, R. (2008). Statistical simulation of wave climate and extreme beach erosion. *Coastal Engineering*, *55*, 375–390. <https://doi.org/10.1016/j.coastaleng.2007.12.003>
- Camus, P., Méndez, F. J., Losada, I. J., Menéndez, M., Espejo, A., Pérez, J., et al. (2014). A method for finding the optimal predictor indices for local wave climate conditions. *Ocean Dynamics*, *64*(7), 1025–1038. <https://doi.org/10.1007/s10236-014-0737-2>
- Camus, P., Menéndez, M., Méndez, F. J., Izaguirre, C., Espejo, A., Cánovas, V., et al. (2014). A weather-type statistical downscaling framework for ocean wave climate. *Journal of Geophysical Research, Oceans*, *119*, 7389–7405. <https://doi.org/10.1002/2014JC010141>
- Chiri, H., Abascal, A. J., Castanedo, S., Antolínez, J. A. A., Liu, Y., Weisberg, R. H., & Medina, R. (2019). Statistical simulation of ocean current patterns using autoregressive logistic regression models: A case study in the Gulf of Mexico. *Ocean Modelling*. <https://doi.org/10.1016/j.ocemod.2019.02.010>
- Cohn, N., Ruggiero, P., García-Medina, G., Anderson, D., Serafin, K., & Biel, R. (2019). Environmental and morphologic controls on wave induced dune response. *Geomorphology*, *329*, 108–128. <https://doi.org/10.1016/j.geomorph.2018.12.023>
- Coles, S. G. (2001). *An Introduction to Statistical Modeling of Extreme Values*, (Vol. 208). London, U. K.: Springer.
- Corbella, S., & Stretch, D. (2013). Simulating a multivariate sea storm using Archimedean copulas. *Coastal Engineering*, *76*, 68–78. <https://doi.org/10.1016/j.coastaleng.2013.01.011>
- Del-Rosal-Salido, J., Folgueras, P., Ortega-Sanchez, M., & Losada, M. (2019). Beyond flood probability assessment: An integrated approach for characterizing extreme water level along transitional environments. *Coastal Engineering*, *152*. <https://doi.org/10.1016/j.coastaleng.2019.103512>
- Efron, B., & Tibshirani, R. (1986). Bootstrap methods for standard errors, confidence intervals, and other measures of statistical accuracy. *Statistical Science*, *54*–57. <https://doi.org/10.1214/ss/1177013815>
- Erikson, L. H., Espejo, A., Barnard, P. L., Serafin, K. A., Hegermiller, C. A., O'Neill, A., et al. (2018). Identification of storm events and contiguous coastal sections for deterministic modeling of extreme coastal flood events in response to climate change. *Coastal Engineering*, *140*, 316–330. <https://doi.org/10.1016/j.coastaleng.2018.08.003>
- Godoi, V. A., de Andrade, F. M., Bryan, K., & Gorman, R. M. (2019). Regional-scale ocean wave variability associated with El Niño–Southern Oscillation–Madden-Julian Oscillation combined activity. *International Journal of Climatology*, *39*, 483–494. <https://doi.org/10.1002/joc.5823>
- Gouldby, B., Méndez, F. J., Guanache, Y., Rueda, A., & Mínguez, R. (2014). A methodology for deriving extreme nearshore sea conditions for structural design and flood risk analysis. *Coastal Engineering*, *88*, 15–26. <https://doi.org/10.1016/j.coastaleng.2014.01.012>
- Guanache, Y., Mínguez, R., & Méndez, F. J. (2013). Autoregressive logistic regression applied to atmospheric circulation patterns. *Climate Dynamics*, *42*(1–2), 537–552. <https://doi.org/10.1007/s00382-013-1690-3>
- Gutierrez, J. M., San-Martin, D., Brands, S., Manzanar, R., & Herrera, S. (2013). Reassessing statistical downscaling techniques for their robust application under climate change conditions. *Journal of Climate*, *26*(1), 171–188.
- Haigh, I., MacPherson, L., Mason, M., Wijeratne, E., Pattiaratchi, C., Crompton, R., & George, S. (2014). Estimating present day extreme water level exceedance probabilities around the coastline of Australia: Tropical cyclone-induced storm surges. *Climate Dynamics*, *42*, 139–157. <https://doi.org/10.1007/s00382-012-1653-0>

- Haigh, I., Nicholls, R., & Wells, N. (2010). A comparison of the main methods for estimating probabilities of extreme still water levels. *Coastal Engineering*, 57(9), 838–849. <https://doi.org/10.1016/j.coastaleng.2010.04.002>
- Hannachi, A., & Legras, B. (1995). Simulated annealing and weather regimes classification. *Tellus*, 47A, 955–973. <https://doi.org/10.1034/j.1600-0870.1995.00203.x>
- Hawkes, P. J., Gouldby, B. P., Tawn, J. A., & Owen, M. W. (2002). The joint probability of waves and water levels in coastal engineering design. *Journal of Hydraulic Research*, 40(3), 241–251. <https://doi.org/10.1080/00221680209499940>
- Hegermiller, C. A., Antolinez, J. A. A., Rueda, A., Camus, P., Perez, J., Erikson, L. H., et al. (2017). A multimodal wave spectrum-based approach for statistical downscaling of local wave climate. *American Meteorological Society*, 47(February), 375–386. <https://doi.org/10.1175/JPO-D-16-0191.1>
- Henderson, S. A., & Maloney, E. D. (2018). The Impact of the Madden-Julian Oscillation on High-Latitude Winter Blocking during El Niño–Southern Oscillation Events. *Journal of Climate*, 31, 5293–5318. <https://doi.org/10.1175/JCLI-D-17-0721.1>
- Hovmöller, E. (1949). The Trough-and-Ridge diagram. *Tellus*, 1, 62–66. <https://doi.org/10.3402/tellusa.v1i2.8498>
- Huang, B., Banzon, V. F., Freeman, E., Lawrimore, J., Liu, W., Peterson, T. C., et al. (2015). Extended Reconstructed Sea Surface Temperature (ERSST), Version 4. NOAA National Centers for Environmental Information. <https://doi.org/10.7289/V5KD1VVF> [08/2018].
- Huang, W., Xu, S., & Nnaji, S. (2008). Evaluation of GEV model for frequency analysis of annual maximum water levels in the coast of United States. *Ocean Engineering*, 35, 1132–1147. <https://doi.org/10.1016/j.oceaneng.2008.04.010>
- Hunter, J. (2011). A simple technique for estimating an allowance for uncertain sea-level rise. *Climatic Change*, 113(2), 239–252. <https://doi.org/10.1007/s10584-011-0332-1>
- Huth, R., Beck, C., Philipp, A., Demuzere, M., Ustrnul, Z., Cahynová, M., et al. (2008). Classifications of atmospheric circulation patterns. *Trends and Directions in Climate Research*, 1146, 105–152. <https://doi.org/10.1196/annals.1446.019>
- Jankowski, K. L., Tornqvist, T. E., & Fernandes, A. M. (2017). Vulnerability of Louisiana's coastal wetlands to present-day rates of relative sea-level rise. *Nature Communications*, 8, 1–7. <https://doi.org/10.1038/ncomms14792>
- Lafleur, D. M., Barrett, B. S., & Henderson, G. R. (2015). Some climatological aspects of the Madden-Julian Oscillation (MJO). *Journal of Climate*, 28, 6039–6053.
- Landsea, C. W., & Franklin, J. L. (2013). Atlantic hurricane database uncertainty and presentation of a new database format. *Monthly Weather Review*, 141, 3576–3592. <https://doi.org/10.1175/mwr-d-12-00254.1>
- Le Cozannet, G., Rohmer, J., Cazenave, A., Idier, D., van de Wal, R., De Winter, R., et al. (2015). Evaluating uncertainties of future marine flooding occurrence as sea-level rises. *Environmental Modeling and Software*, 73, 44–56. <https://doi.org/10.1016/j.envsoft.2015.07.021>
- Leonard, M., Westra, S., Phatak, A., Lambert, M., van den Hurk, B., McInnes, K., et al. (2014). A compound event framework for understanding extreme impacts. *Wiley Interdisciplinary Reviews: Climate Change*, 5(1), 113–128. <https://doi.org/10.1002/wcc.252>
- Ludka, B. C., Gallien, T. W., Crosby, S. C., & Guza, R. T. (2016). Mid-El Niño erosion at nourished and unnourished Southern California beaches. *Geophysical Research Letters*, 43, 4510–4516. <https://doi.org/10.1002/2016GL068612>
- Ludka, B. C., Guza, R. T., O'Reilly, W. C., & Yates, M. L. (2015). Field evidence of beach profile evolution toward equilibrium. *Journal of Geophysical Research*, Oceans, 120, 7574–7597. <https://doi.org/10.1002/2015JC010893>
- MacPherson, L. R., Arns, A., Dangendorf, S., Vafeidis, A. T., & Jensen, J. (2019). A stochastic extreme sea level model for the German Baltic Sea Coast. *Journal of Geophysical Research: Oceans*, 124(3), 2054–2071. <https://doi.org/10.1029/2018JC014718>
- Madden, R. A., & Julian, P. R. (1972). Description of global-scale circulation cells in the tropics with a 40–50 day period. *Journal of the Atmospheric Sciences*, 29, 1109–1123. [https://doi.org/10.1175/1520-0469\(1972\)029<1109:dogsc>2.0.co;2](https://doi.org/10.1175/1520-0469(1972)029<1109:dogsc>2.0.co;2)
- Marcos, M., Calafat, F., Berihuete, A., & Dangendorf, S. (2015). Long-term variations in global sea level extremes. *Journal of Geophysical Research*, Oceans, 120, 8115–8134. <https://doi.org/10.1002/2015JC011173>
- Marcos, M., Rohmer, J., Vousdoukas, M., Mentaschi, L., Cozannet, G. L., & Amores, A. (2019). Increase extreme coastal water levels due to the combined action of storm surges and wind-waves. *Geophysical Research Letters*. <https://doi.org/10.1029/2019GL082599>
- Marshall, A. G., Hendon, H. H., Durrant, T. H., & Hemer, M. A. (2015). Madden Julian Oscillation impacts on global ocean surface waves. *Ocean Modelling*, 96, 136–147. <https://doi.org/10.1016/j.oceomod.2015.06.002>
- Masina, M., Lamberti, A., & Archetti, R. (2015). Coastal flooding: A copula based approach for estimating the joint probability of water levels and waves. *Coastal Engineering*, 97, 37–52. <https://doi.org/10.1016/j.coastaleng.2014.12.010>
- Méndez, F. J., Menéndez, M., Luceño, A., & Losada, I. L. (2006). Estimation of the long-term variability of extreme significant wave height using a time-dependent Peak Over Threshold (POT) model. *Journal of Geophysical Research*, Oceans, 111, C07024. <https://doi.org/10.1029/2005JC003344>
- Menéndez, M., & Woodworth, P. L. (2010). Changes in extreme high water levels based on a quasi-global tide-gauge data set. *Journal of Geophysical Research*, Oceans, 115, C10011. <https://doi.org/10.1029/2009JC005997>
- Mentaschi, L., Vousdoukas, M., Voukouvalas, E., Dosio, A., & Feyen, L. (2017). Global changes of extreme coastal wave energy fluxes triggered by intensified teleconnection patterns. *Geophysical Research Letters*, 44, 2416–2426. <https://doi.org/10.1002/2016GL072488>
- Merrifield, M. A., Thompson, P. R., & Lander, M. (2012). Multidecadal sea level anomalies and trends in the western tropical Pacific. *Geophysical Research Letters*, 39. <https://doi.org/10.1029/2012GL05032>
- Muis, S., Verlaan, M., Winsemius, H., Aerts, J., & Ward, P. (2016). A global reanalysis of storm surges and extreme sea levels. *Nature Communications*, 9. <https://doi.org/10.1038/ncomms11969>
- Nerem, R. S., Beckley, B. D., Fasullo, J. T., Hamlington, B. D., Masters, D., & Mitchum, G. T. (2018). Climate-change-driven accelerated sea level rise detected in the altimeter era. *Proceedings of the National Academy of Sciences*, 115(9), 2022–2025. <https://doi.org/10.1073/pnas.1717312115>
- Neumann, B., Vafeidis, A. T., Zimmermann, J., & Nicholls, R. J. (2015). Future coastal population growth and exposure to sea-level rise and coastal flooding—A global assessment. *PLoS ONE*, 10(3), e0118571. <https://doi.org/10.1371/journal.pone.0118571>
- Parker, K., Ruggiero, P., Serafin, K., & Hill, D. (2019). Emulation as an approach for rapid estuarine modeling. *Coastal Engineering*, 150, 79–93. <https://doi.org/10.1016/j.coastaleng.2019.03.004>
- Pawlowicz, R., Beardsley, B., & Lentz, S. (2002). Classical tidal harmonic analysis including error estimates in MATLAB using T_TIDE. *Computers and Geosciences*, 28, 929–937. [https://doi.org/10.1016/S0098-3004\(02\)00013-4](https://doi.org/10.1016/S0098-3004(02)00013-4)
- Perez, J., Méndez, F. J., Menéndez, M., & Losada, I. J. (2014). ESTELA: A method for evaluating the source and travel time of the wave energy reaching a local area. *Ocean Dynamics*, 64(8), 1181–1191. <https://doi.org/10.1007/s10236-014-0740-7>
- Perez, J., Menéndez, M., Camus, P., Méndez, F. J., & Losada, I. J. (2015). Statistical multi-model climate projections of surface ocean waves in Europe. *Ocean Modelling*, 96, 161–170. <https://doi.org/10.1016/j.oceomod.2015.06.001>
- Perez, J., Menéndez, M., & Losada, I. J. (2017). GOW2: A global wave hindcast for coastal applications. *Coastal Engineering*, 124, 1–11. <https://doi.org/10.1016/j.coastaleng.2017.03.005>

- Philander, S. G. H. (1983). El Niño Southern Oscillation phenomena. *Nature*, *302*, 295–301. <https://doi.org/10.1038/302295a0>
- Philipp, A., Beck, C., Huth, R., & Jacobeit, J. (2016). Development and comparison of circulation type classifications using the COST 733 dataset and software. *International Journal of Climatology*. <https://doi.org/10.1002/joc.3920>
- Plomaritis, T. A., Benavente, J., Laiz, I., & Del Río, L. (2015). Variability in storm climate along the Gulf of Cadiz: The role of large scale atmospheric forcing and implications to coastal hazards. *Climate Dynamics*, *45*, 2499–2514. <https://doi.org/10.1007/s00382-0150248604>
- Poelhekke, L., Jäger, W. S., van Dongeren, A., Plomaritis, T. A., McCall, R., & Ferreira, Ó. (2016). Predicting coastal hazards for sandy coasts with a Bayesian Network. *Coastal Engineering*, *118*, 21–34. <https://doi.org/10.1016/j.coastaleng.2016.08.011>
- Rasche, N., & Arduin, F. (2013). A global wave parameter database for geophysical applications. Part 2: Model validation with improved source term parameterization. *Ocean Modelling*, *70*, 174–188. <https://doi.org/10.1016/j.ocemod.2012.12.001>
- Ray, R. D., & Foster, G. (2016). Future nuisance flooding at Boston caused by astronomical tides alone. *Earth's Future*, *4*, 578–587. <https://doi.org/10.1002/2016EF000423>
- Rueda, A., Camus, P., Tomas, A., Vitousek, S., & Méndez, F. J. (2016). A multivariate extreme wave and storm surge climate emulator based on weather patterns. *Ocean Modelling*, *104*, 242–251. <https://doi.org/10.1016/j.ocemod.2016.06.008>
- Rueda, A., Hegermiller, C. A., Antolinez, J. A. A., Camus, P., Vitousek, S., Ruggiero, P., et al. (2017). Multiscale climate emulator of multimodal wave spectra: MUSCLE-spectra. *Journal of Geophysical Research, Oceans*, *122*, 1400–1415. <https://doi.org/10.1002/2016JC011957>
- Rueda, A., Vitousek, S., Camus, P., Tomás, A., Espejo, A., Losada, I. J., et al. (2017). A global classification of coastal flood hazard climates associated with large-scale oceanographic forcing. *Scientific Reports*, *7*(1), 1–8. <https://doi.org/10.1038/s41598-017-05090-w>
- Ruggiero, P., Komar, P. D., McDougal, W. G., Marra, J. J., & Beach, R. (2001). Wave runup, extreme water levels and the erosion of properties backing beaches. *Journal of Coastal Research*, *17*, 407–419. <https://doi.org/10.1061/9780784402429.216>
- Saha, S., Moorthi, S., Wu, X., Wang, J., Nadiga, S., Tripp, P., et al. (2011). *NCEP Climate Forecast System Version 2 (CFSv2) Selected Hourly Time-Series Products*. Research data archive at the National Center for Atmospheric Research, Computational and Information Systems Laboratory. <https://doi.org/10.5065/D6N877VB>
- Sallenger, A. H. (2000). Storm impact scale for barrier islands. *Journal of Coastal Research*, *16*(3), 890–895.
- Serafin, K. A., & Ruggiero, P. (2014). Simulating extreme total water levels using a time-dependent, extreme value approach. *Journal of Geophysical Research, Oceans*, *119*, 6305–6329. <https://doi.org/10.1002/2014JC010093>
- Serafin, K. A., Ruggiero, P., Barnard, P., & Stockdon, H. F. (2019). The influence of shelf bathymetry and beach topography on extreme total water levels: Linking large-scale changes of the wave climate to local coastal hazards. *Coastal Engineering*. <https://doi.org/10.1016/j.coastaleng.2018.03.012>
- Serafin, K. A., Ruggiero, P., & Stockdon, H. F. (2017). The relative contribution of waves, tides, and nontidal residuals to extreme total water levels on U.S. West Coast sandy beaches. *Geophysical Research Letters*, *44*, 1839–1847. <https://doi.org/10.1002/2016GL071020>
- Sheridan, S. C., & Lee, C. C. (2011). The self-organizing map in synoptic climatological research. *Progress in Physical Geography*, *35*(1), 109–119. <https://doi.org/10.1177/0309133310397582>
- Sheridan, S. C., Lee, C. C., Adams, R. E., Smith, E. T., Pirhalla, D. E., & Ransibrahmanakul, V. (2019). Temporal modeling of anomalous coastal sea level values using synoptic climatological patterns. *Journal of Geophysical Research, Oceans*, *124*. <https://doi.org/10.1029/2019JC015421>
- Slade, S. A., & Maloney, E. D. (2013). An intraseasonal prediction model of Atlantic and East Pacific tropical cyclone genesis. *Monthly Weather Review*, *141*, 1925–1942. <https://doi.org/10.1175/MWR-D-12-00268.1>
- Stockdon, H. F., Holman, R. A., Howd, P. A., & Sallenger, A. H. (2006). Empirical parameterization of setup, swash, and runup. *Coastal Engineering*, *53*(7), 573–588. <https://doi.org/10.1016/j.coastaleng.2005.12.005>
- Sweet, W. V., Kopp, R. E., Weaver, C. P., Obeysekera, J., Horton, R. M., et al. (2017). Global and regional sea level rise scenarios for the United States. NOAA Technical Report NOS CO-OPS 083
- Sweet, W. V., & Park, J. (2014). From the extreme to the mean: Acceleration and tipping points of coastal inundation from sea level rise. *Earth's Future*, *2*, 578–600. <https://doi.org/10.1002/2014EF000272>
- Tang, Y., & Yu, B. (2008). MJO and its relationship to ENSO. *Journal of Geophysical Research-Atmospheres*, *113*, D14106. <https://doi.org/10.1029/2007jd009230>
- Vitousek, S., Barnard, P. L., & Limber, P. (2017). Can beaches survive climate change. *Journal of Geophysical Research, Earth Surface*, *122*, 1060–1067. <https://doi.org/10.1002/2017JF004308>
- Vousdoukas, M., Mentaschi, L., Voukouvalas, E., Verlaan, M., Jevrejeva, S., Jackson, L., & Feyen, L. (2018). Global probabilistic projections of extreme sea levels show intensification of coastal flood hazard. *Nature Communications*, *9*(1), p2360. <https://doi.org/10.1038/s41467-018-04692-w>
- Vousdoukas, M., Voukouvalas, E., Mentaschi, L., Dottori, F., Giardino, A., Bouziotas, D., et al. (2016). Developments in large-scale coastal flood hazard mapping. *Natural Hazards and Earth System Sciences*, *16*, 1841–1853. <https://doi.org/10.5194/nhess-16-1841-2016>
- Wahl, T., & Chambers, D. (2015). Evidence for multidecadal variability in US extreme sea level records. *Journal of Geophysical Research, Oceans*, *120*, 1527–1544. <https://doi.org/10.1002/2014JC010443>
- Wahl, T., Haigh, I. D., Nicholls, R. J., Arns, A., Dangendorf, S., Hinkel, J., & Slangen, A. B. A. (2017). Understanding extreme sea levels for broad-scale coastal impact and adaptation analysis. *Nature Communications*, *8*. <https://doi.org/10.1038/ncomms16075>
- Wahl, T., Muddersback, C., & Jensen, J. (2012). Assessing the hydrodynamic boundary conditions for risk analyses in coastal areas: A multivariate statistical approach based on Copula functions. *Natural Hazards and Earth Systems Science*, *12*, 495–510. <https://doi.org/10.5194/nhess-12-495-2012>
- Wahl, T., & Plant, N. G. (2015). Changes in erosion and flooding risk due to long-term and cyclic oceanographic trends. *Geophysical Research Letters*, *42*, 2943–2950. <https://doi.org/10.1002/2015GL063876>
- Wheeler, M. C., & Hendon, H. H. (2004). An all-season real-time multivariate MJO index: Development of an index for monitoring and prediction. *Monthly Weather Review*, *132*, 1917–1932. [https://doi.org/10.1175/1520-0493\(2004\)132<1917:aarmmi>2.0.co;2](https://doi.org/10.1175/1520-0493(2004)132<1917:aarmmi>2.0.co;2)
- Williams, I. N., & Patricola, C. M. (2018). Diversity of ENSO events unified by convective threshold sea surface temperature: A nonlinear ENSO index. *Geophysical Research Letters*, *45*. <https://doi.org/10.1029/2018/GL079203>